Inorganic Chemistry

pubs.acs.org/IC

Article

Assembly of Polyiodide Networks with Cu(II) Complexes of Pyridinol-Based Tetraaza Macrocycles

Álvaro Martínez-Camarena,[‖] Matteo Savastano,[‖] Salvador Blasco, Estefanía Delgado-Pinar, Claudia Giorgi, Antonio Bianchi,* Enrique García-España,* and Carla Bazzicalupi

Cite This: *Inorg. Chem.* 2022, 61, 368−383

Read Online

ACCESS | Metrics & More | Article Recommendations | Supporting Information

ABSTRACT: Polyiodide networks are currently of great practical interest for the preparation of new electronic materials. The participation of metals in the formation of these networks is believed to improve their mechanical performance and thermal stability. Here we report the results on the construction of polyiodide networks obtained using Cu(II) complexes of a series of pyridinol-based tetraazacyclophanes as countercations. The assembly of these crystalline polyiodides takes place from aqueous solutions on the basis of similar structural elements, the $[CuL]^{2+}$ and $[Cu(H_{-1}L)]^{+}$ (L = **L2**, **L2-Me**, **L2-Me$_3$**) complex cations, so that the peculiarities induced by the increase of N-methylation of ligands, the structural variable of ligands, can be highlighted. First, solution equilibria involving ligands and complexes were analyzed (potentiometry, NMR, UV−vis, ITC). Then, the appropriate conditions could be selected to prepare polyiodides based on the above complex cations. Single-crystal XRD analysis showed that the coordination of pyridinol units to two metal ions is a prime feature of these ligands, leading to polymeric coordination chains of general formula $\{[Cu(H_{-1}L)]\}_n^{n+}$ (L = **L2-Me**, **L2-Me$_3$**). In the presence of the I^-/I_2 couple, the polymerization tendency stops with the formation of $[(CuL)(CuH_{-1}L)]^{3+}$ (L = **L2-Me**, **L2-Me$_3$**) dimers which are surrounded by polyiodide networks. Moreover, coordination of the pyridinol group to two metal ions transforms the surface charge of the ring from negative to markedly positive, generating a suitable environment for the assembly of polyiodide anions, while N-methylation shifts the directional control of the assembly from H-bonds to I···I interactions. In fact, an extended concatenation of iodine atoms occurs around the complex dimeric cations, the supramolecular I···I interactions become shorter and shorter, fading into stronger forces dominated by the orbital overlap, which is promising for effective electronic materials.

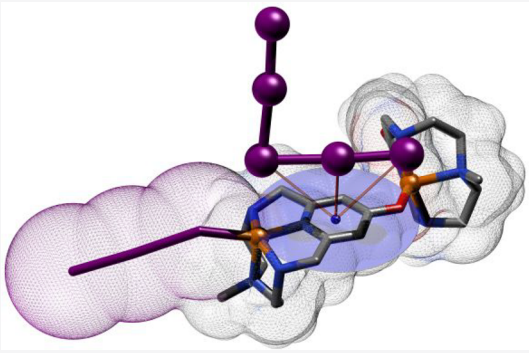

■ INTRODUCTION

Small polyazacycloalkanes have aroused a great interest since the earliest years of macrocyclic chemistry, as the convergent arrangement of their donor atoms allows for strong complexation of many transition-metal ions. The early inclusion of N-heterocyclic, aromatic groups into their macrocyclic structures introduced several additional properties related to ligand rigidity, modulation of binding characteristics, implementation of π-interactions, and activation of mechanisms, based on the absorption and/or the emission properties of N-heteroaromatic groups, to sense and report the interactions with guest species.[1]

A noteworthy member of this class of macrocyclic ligands is 3,6,9-triaza-1-(2,6)-pyridinacyclodecaphane (**L1**, Figure 1) which, in the three decades since its appearance,[2] has given rise to a large family of derivatives that have been investigated for applications in many areas, including, among others, pharmaceutical and biomedical sectors,[3−17] catalysis,[18−23] and chemosensing[24−27] as well as in the preparation of polybromides[28] and polyiodides[29,30] featuring iodine-dense three-dimensional networks that might open up new perspectives in crystal engineering and in the design of solid-state conductors as well as in the preparation of new chemicals with antimicrobial activity.[31−33]

A considerable part of these applications involved metal complexes and exploited free coordination positions on metal ions as active sites: **L1** and many of its derivatives do not contain enough donor atoms to fulfill metal coordination spheres. We have recently shown,[30] for instance, that metal centers in Cu(II) complexes of **L1** and its methylated derivatives **L1-Me** and **L1-Me$_3$** (Figure 1) can aid in the formation of particular polyiodide networks that are assembled from simple tectons, such as I^- and I_2, passing through complex I_3^-, I_5^-, and I_7^- anions and the unusual I_8^{2-} species which connects two Cu(II) centers.

Received: September 23, 2021
Published: December 22, 2021

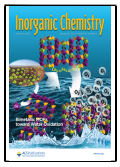

ACS Publications

© 2021 The Authors. Published by American Chemical Society

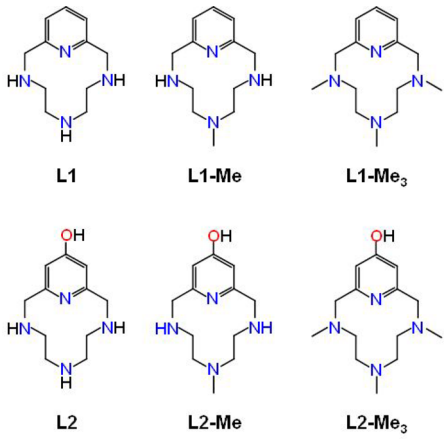

Figure 1. Ligands drawing.

Many metals can participate in the formation of iodine chains.[34] They are thought to enhance the mechanical performance and the thermal stability of polyiodides and, as recently shown,[35] to modulate their conduction properties. I···I interactions, in addition to being an opportunity for semantic considerations,[36] are the connectors that can make solid-state conduction feasible and efficient based on a Grotthuss-like mechanism,[37,38] which requires the preservation of orbital overlap along the iodine chains, a phenomenon favored by high iodine density.[37,39,40] Nonetheless, it has been shown that the physical properties, that is, electrical conductivity and thermal stability, of polyiodide chains are also affected by the supramolecular interactions they experience in the crystals.[41] These details form a basis of information that can aid in the design of high-performance polyiodide-based solid-state conductors, which are of currently great practical interest for the development of new devices, especially for the preparation of solar cells[42,43] and batteries.[44,45]

The progressive N-methylation of the ligand, from **L1** to **L1-Me** and **L1-Me$_3$**, offered the opportunity to observe the effect of the transition to less polar environments around the metal centers.[30] The loss of H-bond donor groups causes a shift from the hydrogen-bond domain to that of I···I interactions, in terms of the main forces participating in the organization of the crystalline phases, that is accompanied by the greater participation of Cu(II) ions in the stabilization of the polyiodide network.

Modifications of the electron density of the pyridine group could be another tool for fine-tuning the metal coordination properties of these ligands and the propagation of their electronic properties to the surrounding polyiodide networks either by direct connection to the metal ions (polyiodide coordination) and by proximity to surfaces of modified electron density. Nevertheless, only few examples of pyridine-substituted derivatives of **L1**, **L1-Me**, and **L1-Me$_3$**, bearing both electron-donating and electron-withdrawing groups, have been reported, so far.[29,46−48] Among these, only **L2-Me$_3$** (Figure 1) has been used for the preparation of polyiodides, in the absence of metal ions, leading to the [H$_2$**L2-Me$_3$**(I$_7$)$_2$] compound featuring diprotonated ligand molecules segregated into boxes formed by couples of tripodal I$_7^-$ anions.[29] Analysis of its crystal structure led us to believe that the formation of these rare I$_7^-$ anions is due to the capacity of (H$_2$**L2-Me$_3$**)$^{2+}$ to act as a supramolecular templating agent, molding the heptaiodide anion around itself. This arrangement of polyiodide units, despite forming a dense iodine lattice (iodine number I_N = 0.589 for [H$_2$**L2-Me$_3$**(I$_7$)$_2$]),[49] does not allow for the formation of an extended iodine network which is a mandatory requirement for solid state conduction.

In this paper, we analyze the formation of Cu(II) complexes with the pyridinol ligands **L2**, **L2-Me**, and **L2-Me$_3$** and the extended and dense polyiodide networks we have built around these complexes. The **L2**-based ligands reproduce the progressive N-methylation of the **L1**-based analogues, while the presence of the *para* −OH group introduces two additional factors: (i) the possibility of intermolecular interactions (formation of oligomeric complexes or coordination polymers) via coordinative/hydrogen bonding of deprotonated/protonated −OH groups and (ii) alteration of the electronic properties of the pyridine ring brought about by this *para* substituent. With respect to the latter, the *para* −OH group increases the electron density on the pyridine ring,[48] a phenomenon that would seem to generate an adverse environment for the stabilization of polyiodide anions. Nevertheless, metal coordination to the pyridinol nitrogen atom facilitates the deprotonation of this −OH group and the polarization of the ring electron density toward the N-coordinated metal ion, through the stabilization of the ketone ligand form.[17] Further depletion of ring electron density is expected to occur if the ketone oxygen is also involved in the coordination of a metal ion, thus creating favorable conditions for the stabilization of polyiodides via anion-π interactions, as actually found with the study herewith described.

■ EXPERIMENTAL SECTION

Materials. ***Caution!*** *Solid perchlorate salts and their nonaqueous solutions are potentially explosive and should be handled in small quantities.*

All reagents were purchased from commercial sources and used as received. Solvents were of analytical grade and used without further purification. Water used for potentiometric and spectroscopic measurements was twice distilled and passed through a Millipore apparatus.

Ligands 3,6,9-triaza-1(2,6)-pyridinecyclodecaphan-1^4-ol (**L2**),[46] 6-(*N*-methyl)-3,6,9-triaza-1(2,6)-pyridinecyclodecaphan-1^4-ol (**L2-Me**),[29] and 3,6,9-tris(*N*-methyl)-3,6,9-triaza-1(2,6)-pyridinecyclodecaphan-1^4-ol (**L2-Me$_3$**)[29] were synthesized as previously described.

Crystals of [Cu(H$_{-1}$**L2-Me**)](ClO$_4$)·0.716H$_2$O (**1**) and [Cu(H$_{-1}$**L2-Me$_3$**)](ClO$_4$)·H$_2$O (**2**) were obtained by slow evaporation at room temperature of aqueous solutions containing equimolar quantities of ligand (**L2-Me** or **L2-Me$_3$**) and Cu(ClO$_4$)$_2$·6H$_2$O at pH = 7. Complex **1**: yield: 63%. Elemental analysis: calcd (%) for $C_{24}H_{41}Cl_2Cu_2N_8O_{12}$: C, 34.66; H, 4.97; N, 13.47. Found: C, 34.71; H, 5.09; N, 13.49. Complex **2**: yield: 74%. Elemental analysis: calcd (%) for $C_{28}H_{48}Cl_2Cu_2N_8O_{11}$: C, 38.62; H, 5.56; N, 12.87. Found: C, 38.57; H, 5.50; N, 12.93.

Crystals of {[(Cu**L2-Me**)(CuH$_{-1}$**L2-Me**)I]·[(Cu**L2-Me**)(CuH$_{-1}$**L2-Me**)]I$_3$}(I$_2$)(I$_5$)$_3$(I$_7$) (**3**) and [(Cu**L2-Me$_3$**)(CuH$_{-1}$**L2-Me$_3$**)I](I$_2$)$_2$(I$_5$)$_2$ (**4**) were obtained by slow diffusion, at room temperature, of aqueous solutions of complexes **1** and **2** toward iodine rich I$_2$/I$^-$ aqueous mixtures (I$_2$:I$^-$ ratio 2:1) inside H-shaped tubes. The solutions' pH was about 6. The H-shaped tubes were loaded with 0.01 mmol of the complex on one side and an excess of the I$_2$/I$^-$ mixtures (I$_2$ 0.1 mmol, NaI 0.05 mmol) on the other side. Crystals started being formed after about 1 week. After 4 weeks, when the solution into the tube had become uniform in color, crystals were collected by filtration, washed with water, and air dried. Complex **3**: yield: 73%. Elemental analysis: calcd (%) for $C_{48}H_{78}Cu_4I_{28}N_{16}O_4$: C, 12.14; H, 1.66; N, 4.72. Found: C, 12.21; H, 1.69; N, 4.78. Complex

https://doi.org/10.1021/acs.inorgchem.1c02967
Inorg. Chem. 2022, 61, 368−383

4: yield: 66%. Elemental analysis: calcd (%) for $C_{28}H_{47}Cu_2I_{15}N_8O_2$: C, 13.15; H, 1.85; N, 4.38. Found: C, 13.28; H, 1.88; N, 4.43.

EMF Measurements. The potentiometric titrations were carried out at 298.1 ± 0.1 K, using $NaClO_4$ 0.15 M as supporting electrolyte, in the pH range 2.5−11.0. The experimental procedure (buret, potentiometer, cell, stirrer, microcomputer, etc.) has been fully described elsewhere.[50] The acquisition of the electromotive force (emf) data was performed with the computer program PASAT.[51,52] The reference electrode was an Ag/AgCl electrode in saturated KCl solution. The glass electrode was calibrated as a hydrogen ion concentration probe by titration of previously standardized amounts of HCl with CO_2-free NaOH solutions and the equivalent point determined by the Gran's method,[53,54] which gives the standard potential, $E°$, and the ionic product of water (pK_w = 13.73(1)). The computer program HYPERQUAD[55] was used to fit protonation and stability constants. In all experiments, ligand concentration was about 1.0×10^{-3} M. In complexation experiments, the Cu(II) concentration ranged from 5.0×10^{-4} M to 1.0×10^{-3} M. Due to the very high stability of the complexes with **L2-Me** and **L2-Me$_3$**, the polyamine 1,4,8,11-tetraazaundecane was used as a competing ligand in 1.0×10^{-3} M concentration. At least two titration experiments (about 100 point each) were performed for each system. The different titration curves for each system were treated both as separated curves and as merged data sets without significant variations of the determined stability constants. The final values were those obtained from the simultaneous treatment of the merged curves. The HYSS[56] program was used to generate the distribution diagrams.

NMR Measurements. The ^{1}H and ^{13}C NMR spectra were recorded on a Bruker Advance DPX300 spectrometer operating at 300.13 MHz for ^{1}H and at 75.47 MHz for ^{13}C. For the ^{1}H spectra, the solvent signal was used as a reference standard. Adjustments to the desired pH were made using drops of DCl or NaOD solutions. The pD was calculated from the measured pH values using the correlation, pH = pD − 0.4.[57]

UV−vis Measurements. UV−vis absorption spectra were recorded with an Agilent 8453 spectrometer. Solvents were of spectroscopic or equivalent grade. The pH of samples was measured with a Metrohm 713 pH meter, and adjustments of the hydrogen ion concentration were made with diluted HCl and NaOH solutions.

Isothermal Titration Calorimetry. Ligand protonation enthalpies were determined in 0.15 M $NaClO_4$ solution by means of a TAM III (TA Instrument) microcalorimeter equipped with a precision Lund syringe pump coupled with a 0.500 cm^3 gastight Hamilton syringe according to a procedure already described.[30] In a typical experiment, a NaOH solution (0.15 M, addition volumes 15 μL) was added to acidic solutions of the ligands (5×10^{-3} M, 1.2 cm^3) in 0.15 M $NaClO_4$. At least two titrations were performed for each system. Corrections for the heats of dilution were applied. The computer program HypCal (updated version of HypΔH)[58] was used to calculate reaction enthalpies from calorimetric data. Ligand protonation constants used in calculations were separately determined by means of potentiometric titrations.

Crystal Structure Determination. Blue crystals of [Cu(H$_{-1}$**L2-Me**)](ClO$_4$)·0.716H$_2$O (**1**) and [Cu(H$_{-1}$**L2-Me$_3$**)](ClO$_4$)·H$_2$O (**2**) and black crystals with metallic luster of {[(Cu**L2-Me**)(CuH$_{-1}$**L2-Me**)I]·[(Cu**L2-Me**)(CuH$_{-1}$**L2-Me**)]I$_3$}(I$_2$)(I$_5$)$_3$(I$_7$) (**3**) and [(Cu**L2-Me$_3$**)(CuH$_{-1}$**L2-Me$_3$**)I](I$_2$)$_2$(I$_5$)$_2$ (**4**) were used for X-ray diffraction (XRD) analysis. A summary of the crystallographic data is reported in Table S1. The integrated intensities were corrected for Lorentz and polarization effects, and an empirical absorption correction was applied for crystals of **3** and **4**.[59] Crystal structures of **1** and **2** were solved by using SHELXD,[60] while SHELXT[61] was used to solve the structures of **3** and **4**. Refinements were performed by means of full-matrix least-squares using SHELXL version 2014/7.[62] Nonhydrogen atoms were anisotropically refined. Hydrogen atoms were introduced as riding atoms with thermal parameter calculated in agreement with the linked atom. In compound **3**, the coordinated iodide ion has been found spread over two positions, which were introduced in the calculation as I28 and I29 iodine atoms and refined with occupation factors equal to 0.65 and 0.35, respectively.

Hirshfeld Surface Analysis. Hirshfeld surface analysis[63−65] was performed with CrystalExplorer17.[66]

Calculation of the ESP Surfaces. The modeling of the trimethylated ligand and its mono- and dimeric Cu(II) complexes was performed using the density functional theory computational method as well as the Becke three-parameter Lee−Yang−Parr hybrid functional.[67−69] All the optimizations were carried out by using the Ahlrichs' basis set def2-TZV(P)[70] for all atoms, including copper. The effect of the polarizable solvent (water) was considered by using the default SCRF method of the polarizable continuum model.[71] Finally, electrostatic potential (ESP) was calculated for each system by means of the Pop = (Esp,ReadRadii) command, considering the atomic radii for Cu(II) of 1.409 Å. Computations were carried out using the program Gaussian 09 C.01.[72] and Molecular graphics and analyses were performed with gMolden[73] and UCSF Chimera, developed by the Resource for Biocomputing, Visualization, and Informatics at the University of California, San Francisco, with support from NIH P41-GM103311.[74]

■ RESULTS AND DISCUSSION

Ligand Protonation Equilibria. The determination of ligand protonation constants is preliminary to the determination of complexation constants and to the speciation of coordination complex systems, which are fundamental information for the preparation of polyiodide complexes. The protonation constants of the pyridinol ligands **L2**, **L2-Me**, and **L2-Me$_3$** were determined by means of potentiometric titrations (0.15 M $NaClO_4$, 298.1 K) and are listed in Table 1 along with those previously obtained[14,16,30] for the pyridine analogues **L1**, **L1-Me**, and **L1-Me$_3$** under the same experimental conditions. Distribution diagrams of the protonated species of **L2** formed as a function of pH are shown in Figure 2, while those corresponding to **L2-Me** and **L2-Me$_3$** can be found in Figure S1.

Table 1. Logarithms of Stepwise Protonation Constants of L2, L2-Me, L2-Me$_3$, L1,[16] L1-Me,[30] and L1-Me$_3$,[14] Obtained by Potentiometric Measurements in 0.15 M $NaClO_4$ at 298.1 ± 0.1 K

reaction[a]	L2	L2-Me	L2-Me$_3$
$H_{-1}L^- + H^+ \rightleftarrows H(H_{-1}L)$	10.89(2)[b]	11.51(2)	10.93(2)
$H(H_{-1}L) + H^+ \rightleftarrows H_2(H_{-1}L)^+$	8.85(1)	8.853(8)	8.25(2)
$H_2(H_{-1}L)^+ + H^+ \rightleftarrows H_2L^{2+}$	5.50(1)	5.718(8)	4.91(2)
$H_2L^{2+} + H^+ \rightleftarrows H_3L^{3+}$	2.27(3)	2.23(4)	−
$\log\beta = \sum\log K$	27.51	28.31	24.10
	L1	**L1-Me**	**L1-Me$_3$**
$L + H^+ \rightleftarrows HL^+$	10.54(1)	10.35(1)	10.88(1)
$HL^+ + H^+ \rightleftarrows H_2L^{2+}$	7.96(1)	8.09(2)	7.37(1)
$H_2L^{2+} + H^+ \rightleftarrows H_3L^{3+}$	1.90(1)	2.47(6)	−
$\log\beta = \sum\log K$	20.40	20.91	18.25

[a]H$_{-1}$L corresponds to the ligands with deprotonated pyridinol moiety. [b]Values in parentheses are standard deviations in the last significant figure.

Protonation constants of **L2** are in good agreement with literature values determined under slightly different experimental conditions (0.15 M NaCl, 298 K).[17]

As can be seen in Table 1, within the investigated pH range (2.5−11), we could determine four protonation constants for **L2** and **L2-Me** and three for **L2-Me$_3$**, that is, protonation of these molecules is characterized by an additional equilibrium, with respect to **L1**, **L1-Me**, and **L1-Me$_3$**, corresponding to the phenol functionalities. The fact that one less constant was found for **L2-Me$_3$**, a phenomenon already observed for **L1-Me$_3$**

https://doi.org/10.1021/acs.inorgchem.1c02967
Inorg. Chem. 2022, 61, 368−383

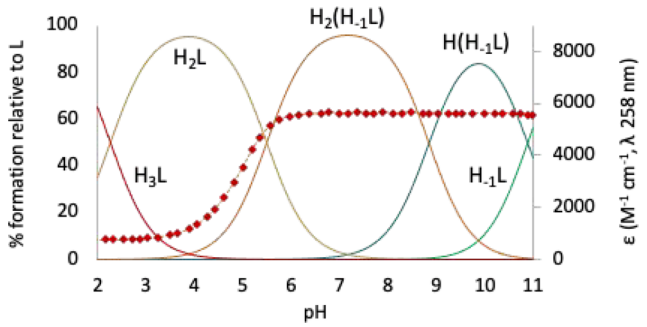

Figure 2. Distribution diagram of the protonated species formed by **L2** as a function of pH in aqueous solution. The extinction coefficient associated with the pyridine band in the UV−vis spectra is represented as red diamonds.

can again be attributed to the significant loss of solvation experienced by the fully methylated ligands, which results in a weaker stabilization of the ammonium groups.[75]

Another outcome of the phenol functionalities is the greater basicity of pyridinol ligands compared to pyridine ones. It is known that deprotonation of the pyridinol OH group establishes a keto−enol equilibrium that enhances the electron density on the pyridine nitrogen atom (Figure 3).[17,47,76] This

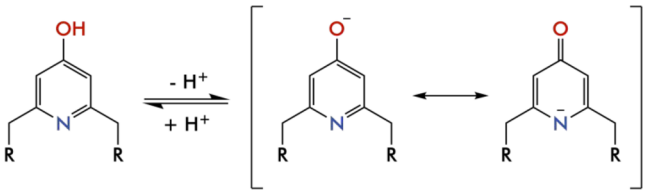

Figure 3. Representation of the keto−enol equilibrium determined for the pyridinol moiety.

leads to a strengthening of the intramolecular hydrogen bond established between the pyridine nitrogen atom and the protonated amines of the macrocycle (Figure 4), thus increasing the value of protonation constants.

The keto−enol equilibrium and the reinforcement of the intramolecular interactions might also explain the particular acidity of this hydroxyl group. The absorbance band of the ketone oxygen (at ca. 270 nm) shows a significant decrease in intensity from pH 6 to 3, as this oxygen atom is protonated (Figures 2 and S1). Similarly, the ^{1}H NMR signals of the

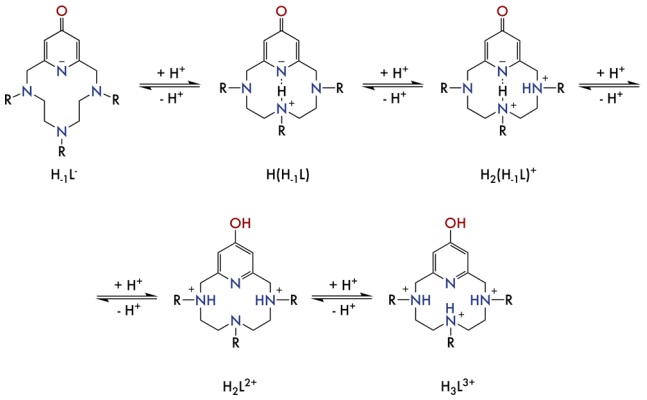

Figure 4. Representation of the protonation sequence proposed for the pyridinol ligands.

aromatic protons shift markedly downfield from pH 6.4 to 3.6 (Figure S2). Hence, both UV and NMR measurements suggest that protonation of the ketone oxygen occurs at about pH 5, which is a particularly low pH for this group (for instance, pK_a is 11.09 for 4-hydroxypyridine, 8.72 for 3-hydroxypyridine, and 11.62 for 2-hydroxypyridine).[77]

In order to fathom the protonation sequence of the macrocycles and to confirm the presence of both the keto−enol equilibrium and the intramolecular hydrogen bonds, we determined the protonation microconstants of **L2-Me** by means of pD titrations followed by ^{1}H NMR. The spectra recorded for **L2-Me** at different pD values can be found in Figure S3. The raw NMR data were treated with the program GEMS based on the implementation of the Cluster Expansion Method.[78] Representation of the variation with pD of the chemical shift of each proton signal, superimposed to the species distribution diagram of the molecules (Figure 5), allowed us to outline some interesting observations.

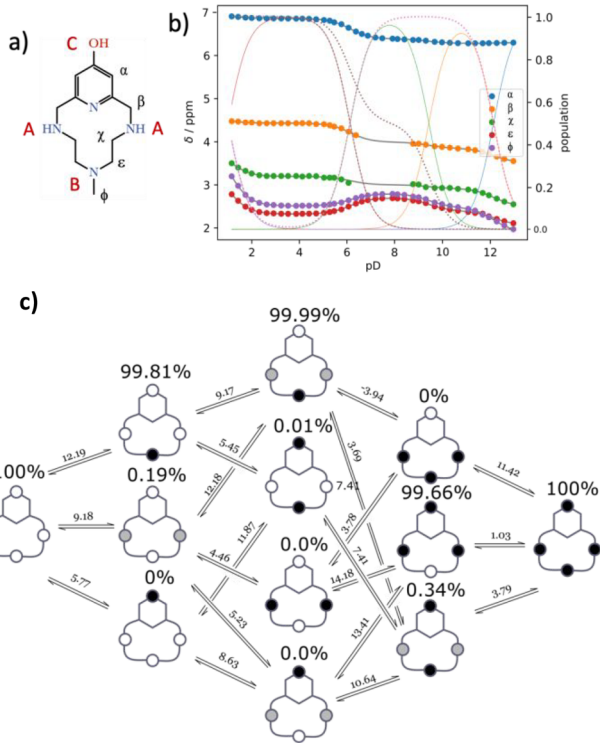

Figure 5. (a) Proton and protonation site labeling. (b) Experimental chemical shifts (scatter plot) and fitted chemical shifts (solid lines). (c) Summary of microstates and microconstants. Black circles represent a protonated site, gray circles represent a delocalized protonation in chemically equivalent sites, and white circles represent a nonprotonated site.

Starting from high pD values and moving toward the acidic zone, it can be noted that the first protonation step takes place at pD ca. 12. This reaction mainly involves the protonation center B, as shown by the upfield movement of hydrogens β, χ, ε, and, mostly, ϕ. This can be easily observed when representing the variation rate of the chemical shifts with pH, shown in Figure S4.

Unlike pyridine ligands, the second protonation of pyridinol macrocycles does not lead to a rearrangement of their protonated amino groups. The introduction of a second hydrogen ion into the molecule involves one of the two

https://doi.org/10.1021/acs.inorgchem.1c02967
Inorg. Chem. 2022, 61, 368−383

Table 2. Thermodynamic Data (kJ mol^{-1}) for Protonation of L2, L2-Me, L2-Me$_3$, L1,[30] L1-Me,[30] and L1-Me$_3$,[30] Determined in 0.15 M $NaClO_4$ at 298.1 ± 0.1 K

reaction[a]	L2		L2-Me		L2-Me$_3$	
	$\Delta H°$	$T\Delta S°$	$\Delta H°$	$T\Delta S°$	$\Delta H°$	$T\Delta S°$
$H_{-1}L^- + H^+ \rightleftarrows H(H_{-1}L)$	−40.2(7)[b]	21.9(7)	−39.9(4)	25.8(4)	−38.8(3)	23.6(3)
$H(H_{-1}L) + H^+ \rightleftarrows H_2(H_{-1}L)^+$	−41.0(8)	9.5(8)	−41.3(4)	9.2(4)	−39.0(3)	7.5(3)
$H_2(H_{-1}L)^+ + H^+ \rightleftarrows H_2L^{2+}$	−22.1(5)	9.2(5)	−24.7(5)	7.9(5)	−10.3(4)	16.8(4)
$H_2L^{2+} + H^+ \rightleftarrows H_3L^{3+}$	−4.0(2)	9.0(3)	−2.1(5)	10.6(5)	–	–
	L1		**L1-Me**		**L1-Me$_3$**	
	$\Delta H°$	$T\Delta S°$	$\Delta H°$	$T\Delta S°$	$\Delta H°$	$T\Delta S°$
$L + H^+ \rightleftarrows HL^+$	−42.6(2)	17.6(2)	−39.5(5)	19.6(5)	−31.3(5)	30.8(5)
$HL^+ + H^+ \rightleftarrows H_2L^{2+}$	−44.6(3)	0.8(3)	−48.3(7)	−2.1(7)	−39.2(6)	−2.9(6)
$H_2L^{2+} + H^+ \rightleftarrows H_3L^{3+}$	−3.1(4)	7.7(4)	0.5(9)	13.4(9)	–	–

[a]$H_{-1}L$ corresponds to the ligands with deprotonated pyridinol moiety. [b]Values in parentheses are standard deviations in the last significant figure.

protonation centers A, while B remains protonated. This is evidenced by the upfield shift of all ^{1}H NMR signals, except α. As previously discussed, the significant stability of the protonated center B can be related to its intramolecular hydrogen-bond interaction with the nitrogen atom of the pyridinol moiety in its ketone form (Figure 4). Therefore, protonation of the ketone oxygen atom is expected to imply a loss of stability which, together with the nearby H^+ at the secondary amino group, should lead to a rearrangement of the protonated amino groups within the macrocycle, a process that actually takes place with the successive protonation step.

Indeed, the third protonation reaction leads to a major rearrangement of the protonated groups: signals ε and ϕ shift downfield, while β, χ, and, significantly, α move upfield, denoting protonation of the C and A centers and deprotonation of B, that is, with the generation of the hydroxyl form of the pyridinol moiety, the protonated center B loses its hydrogen ion in favor of the second center A, thus minimizing the repulsive interactions between positive charges. This explanation is consistent with the results of the UV titrations previously discussed.

Finally, the fourth protonation reaction, occurring at about pD 1, takes place on the only site left available, that is, B, as denoted by the fact that signals χ, ε, and ϕ shift upfield, while α and β keep unchanged.

The analysis of the raw NMR data also allowed us to determine the protonation macroconstants of the **L2-Me**, which can be found in Table S2. The resulting microstates and microconstants are summarized in Figure 5. The correction $pK_D = 0.32 + 1.044\ pK_H$ was applied to the $\log\beta$ obtained by the NMR studies in order to obtain the pK_H values.[57] The obtained logarithmic constants are in reasonable agreement with those determined by the potentiometric titrations, also shown in Table S2, which supports the proposed protonation sequence.

Further characterization of protonation equilibria was performed by means of isothermal titration calorimetry (ITC) measurements to determine the corresponding enthalpy changes ($\Delta H°$), which are listed in Table 2 along with the related entropic contributions ($T\Delta S°$) derived from $-RT\ln K = \Delta H° - T\Delta S°$. For comparison purposes, the analogous data previously determined for **L1**, **L1-Me**, and **L1-Me$_3$** were also included in the same table. Data for the pyridinol ligands **L2**, **L2-Me**, and **L2-Me$_3$** are in keeping with those for their pyridine analogues as well as with the general protonation properties of polyazacycloalkanes,[79] especially with those of polyazacyclophanes[80] bearing a single benzene group in the macrocyclic ring, and are consistent with the fact that the third ligand protonation occurs on the ketone oxygen atom. Indeed, as shown in Table 2, the first two protonation stages are highly exothermic reactions, while the enthalpy contribution for the third stage is much less favorable, as expected for protonation of a phenate oxygen.[81]

In the fourth protonation step (not existing for **L2-Me$_3$**), the poor proton affinity of these ligands is congruent with the almost athermic character of the protonation processes.

All protonation processes are entropically favorable: Ligand protonation causes partial charge neutralization of the bound H^+ ions, which is accompanied by a significant desolvation effect that generates the observed favorable entropy contributions. This phenomenon is commonly observed for similar ligands.[79,80]

Complex Formation with Cu(II). The knowledge of the complex species formed, of their solution abundance, and of their stability under different pH conditions is basilar to establish if a complex system is appropriate for the preparation of polyiodides and, eventually, to select the best synthetic conditions. For this reason, we studied the formation of Cu(II) complexes with **L2**, **L2-Me**, and **L2-Me$_3$** as a function of pH by means of potentiometric titrations. The species formed and the corresponding stability constants we determined by this method are listed in Table 3, where they are compared with

Table 3. Logarithms of the Stability Constants for Cu(II) Complexes of L2, L2-Me, L2-Me$_3$, L1,[30] L1-Me,[30] and L1-Me$_3$,[30] Obtained by Potentiometric Measurements in 0.15 M $NaClO_4$ at 298.1 ± 0.1 K

reaction[a]	L2	L2-Me	L2-Me$_3$
$Cu(II) + L \rightleftarrows [CuL]^{2+}$	13.87(1)[b]	16.13(5)	16.4(1)
$Cu(II) + H_{-1}L^- \rightleftarrows [Cu(H_{-1}L)]^+$	19.35(3)	23.84(4)	23.32(6)
$[Cu(H_{-1}L)]^+ + H_2O \rightleftarrows [Cu(H_{-1}L)(OH)] + H^+$	−9.42(5)	−7.91(3)	−8.46(5)
	L1	**L1-Me**	**L1-Me$_3$**
$Cu(II) + L \rightleftarrows [CuL]^{2+}$	17.78(2)	18.5(1)	16.44(3)
$[CuL]^{2+} + H_2O \rightleftarrows [CuL(OH)]^+ + H^+$	−8.68(8)	−8.73(5)	−8.53(4)
$[CuL(OH)]^+ + H_2O \rightleftarrows [CuL(OH)_2] + H^+$	−10.7(1)	−10.7(2)	−11.31(8)

[a]$H_{-1}L$ corresponds to the ligands with deprotonated pyridinol moiety. [b]Values in parentheses are standard deviations in the last significant figure.

https://doi.org/10.1021/acs.inorgchem.1c02967
Inorg. Chem. 2022, 61, 368−383

the corresponding data previously obtained under the same experimental conditions (0.15 M $NaClO_4$, 298.1 K) for the complexes with **L1**, **L1-Me**, and **L1-Me$_3$**. Distribution diagram of the complex species formed by **L2** is shown in Figure 6,

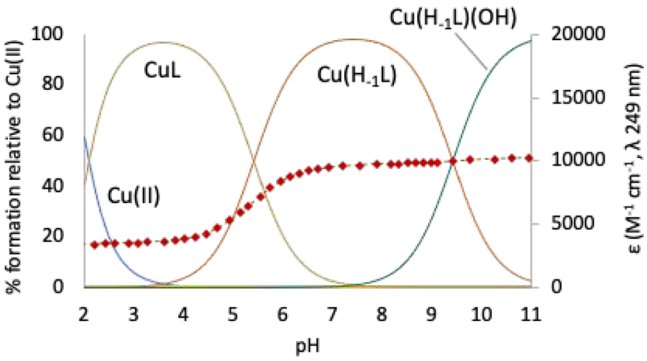

Figure 6. Distribution diagram of the complexes formed in the system Cu(II)/**L2**. [Cu(II)] = [**L2**] = 1 mM. Charges omitted. The extinction coefficient associated with the pyridinol band in the UV−vis spectra recorded at different pH values is represented as red diamonds.

while those corresponding to the complexes formed by **L2-Me** and **L2-Me$_3$** with Cu(II) can be found in Figure S5. The stability constants of **L2** complexes are in good agreement with literature values determined under slightly different experimental conditions (0.15 M NaCl, 298 K).[17]

As can be seen, these complex systems are very simple, being constituted by the three species $[CuL]^{2+}$, $[Cu(H_{-1}L)]^{+}$, and $[Cu(H_{-1}L)(OH)]$ (L = **L2**, **L2-Me**, **L2-Me$_3$**): $H_{-1}L$ corresponds to the ligands with deprotonated pyridinol moiety. An inspection of data in Table 3 indicates some trends of the stability constants. First of all, we can note that, with the exception of trimethylated ligands, pyridinol ligands form $[CuL]^{2+}$ complexes less stable than pyridine ones. In particular, the difference in stability decreases from nonmethylated ($\Delta \log K$ = 4.0 for **L1**, **L2**) to monomethylated ligands ($\Delta \log K$ = 2.4 for **L1-M2**, **L2-Me**) and vanishes for trimethylated ones. Furthermore, the stability constants of these complexes decrease in the order **L2-Me$_3$** ≈ **L2-Me** > **L2** for pyridinol ligands, while the order for pyridine ones is **L1-Me** > **L1** > **L1-Me$_3$**. Most probably, these trends are the result of opposite tendencies induced by the OH substituent on the pyridine rings and by N-methylation of ligands: (i) the electron-donating effect of OH that enhances the donor ability of the pyridinol N atom, (ii) the loss of donor ability by methylated nitrogen atoms due to the loss of M−N−H···O hydrogen bonds with water solvent molecules, and (iii) the lessening of hydration energies of methylated ligands, resulting in a lower cost for desolvation upon complexation.

However, the most notable effect caused by the OH group on Cu(II) complexation is observed when this group is deprotonated. Indeed, deprotonation of the pyridinol moiety dramatically changes the complexation behavior of these ligands by significantly increasing the stability of $[Cu(H_{-1}L)]^{+}$ complexes, relative to $[CuL]^{2+}$ species with both pyridinolic and pyridyl nondeprotonated ligands. Such stability enhancement, which can be related to the above-discussed higher donor character of the N atom of deprotonated pyridinol ligands, is so large (up to ≈7 log units) that in the case of methylated ligands, it was necessary to adopt competition experiments (see Experimental Section) for the determination of complex stability constants. As a consequence, excluding the most acidic pH range (from 2 to 4/5), $H_{-1}L$ is the predominant form of the ligands in their Cu(II) complexes, including the very stable $[Cu(H_{-1}L)(OH)]$ species formed in the alkaline region.

In conclusion, the $[Cu(H_{-1}L)]^{+}$ complexes with **L2**, **L2-Me**, and **L2-Me$_3$** fulfill two fundamental requirements for being promising scaffolds for the preparation of polyiodide: (i) very high stability and (ii) presence of free (solvent occupied) coordination sites on the metal ion. While the first one ensures resistance toward demetalation processes and reduction of Cu(II) to Cu(I) by iodine, the second one favors the binding of exogenous ligands.

A final observation: The deprotonated pyridinolic oxygen atoms of $[Cu(H_{-1}L)]^{+}$ and $[Cu(H_{-1}L)(OH)]$ complexes can act as additional donor atoms favoring intermolecular contacts, an occurrence that was not observed in solution, but was found in the solid state, as shown below.

Crystal Structures. Single crystals of $[Cu(H_{-1}$**L2-Me**$)](ClO_4)\cdot 0.716H_2O$ (**1**) and $[Cu(H_{-1}$**L2-Me$_3$**$)](ClO_4)\cdot H_2O$ (**2**) were subjected to XRD analysis. The asymmetric unit of **1** contains two $[CuH_{-1}$**L2-Me**$]^{+}$ complex cations, two ClO_4^{-} anions (one of which is disordered), and 1.43 H_2O molecules, while one $[Cu(H_{-1}$**L2-Me$_3$**$)]^{+}$, one ClO_4^{-} anion, and one H_2O molecule make up the asymmetric unit of **2**. Both compounds contain polymeric chains of $[Cu(H_{-1}L)]^{+}$ (L = **L2-Me**, **L2-Me$_3$**), extending along the [101] direction, in which the complex units are connected via coordinative interaction of the deprotonated pyridinol oxygen atoms to the Cu(II) ions of neighboring units (Figure 7a,b).

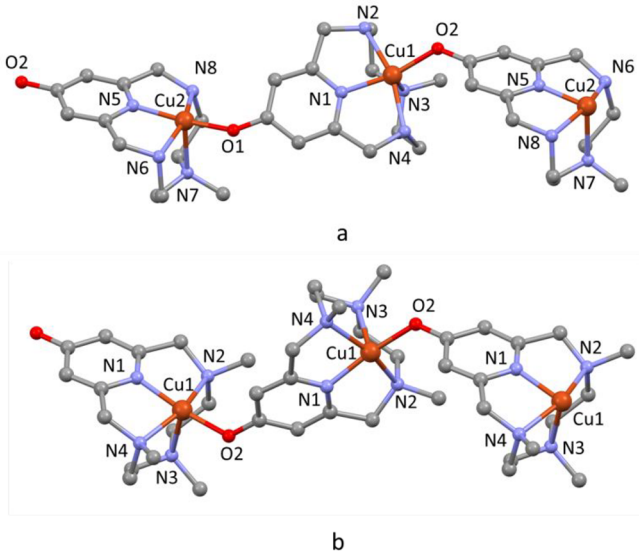

Figure 7. Crystal structures of (a) $[Cu(H_{-1}$**L2-Me**$)](ClO_4)\cdot 0.716H_2O$ (**1**) and (b) $[Cu(H_{-1}$**L2-Me$_3$**$)](ClO_4)\cdot H_2O$ (**2**).

The ligands present a *cis*-folded N_4 configuration, as already observed in similar complexes,[20,30,47,48] so that the nitrogen atom across from the pyridinol group occupies the axial position of the axially elongated square pyramidal coordination environment of Cu(II), while the remaining three ligand nitrogen donors are located in the basal plane along with the pyridinol oxygen atom of the neighboring complex. Coordinative bond distances and angles can be found in Tables S3

https://doi.org/10.1021/acs.inorgchem.1c02967
Inorg. Chem. 2022, 61, 368−383

and S4. The coordinative bonds in the basal plane are in the ranges 1.92−2.10 Å and 1.90−2.14 Å for **1** and **2**, respectively, while those with the apical donors are 2.23 and 2.25 Å for **1** and **2**, respectively. The coordination polymers are helically arranged in the two structures, the $[Cu(H_{-1}L)]^+$ units of the coordination polymers being rotated, with respect to their neighbors, 42.2° in **1** and 80.4° in **2** (as measured by the angle between the mean planes of pyridine rings). This results in a more flat and elongated helix in **1** than in **2** (helix pitch 28 Å vs 14 Å, respectively. Figure S6).

In **1**, symmetry-related polymeric chains, which appear to run in opposite directions, associate in pairs through water bridged H-bonds involving secondary nitrogen and pyridinol oxygen atoms and the formation of $\pi-\pi$ stacking interactions between pyridinol rings coordinated to Cu2 (Figure S7): the separation between the parallel planes of these rings is 3.456 Å, the distance between ring centroids is 3.566 Å, and the displacement of the two centroid is 0.867 Å. Each pair of polymer chains is strengthened by bridging H-bonds with ClO_4^- anions, which also link paired chains with neighboring analogues via direct or H_2O-mediated H-bonds.

Unlike **1**, the polymeric chains of **2** do not give rise to direct interaction with each other, but are separated by perchlorate anions and water molecules that are located in hydrophobic pockets of the lattice surrounded by methyl or methylene groups of ligand molecules with which they form weak H-bonds.

Cu(II) complexes with **L2**, **L2-Me**, and **L2-Me$_3$** were used to prepare polyiodide compounds (see Experimental Section). In the case of **L2-Me** and **L2-Me$_3$**, we obtained crystalline samples suitable for single-crystal XRD analysis. Both contain dinuclear cations formed by the complex units $(CuL)^{2+}$ and $(CuH_{-1}L)^+$ (L = **L2-Me**, **L2-Me$_3$**), joined by coordination of $(CuH_{-1}L)^+$ to $(CuL)^{2+}$ through the deprotonated pyridinol oxygen of the former. A schematic drawing of the overall $[(CuL)(CuH_{-1}L)X]^{2+}$ dinuclear cation (X = I^- or I_3^-) is shown in Scheme 1.

Scheme 1. Schematic Representation of the $[(CuL)(Cu(H_{-1}L))X]^{2+}$ Dinuclear Cation (L = L2-Me; R_1 = H, R_2 = Me; L = L2-Me$_3$; R_1 = R_2 = Me; X = I^- or I_3^-) Found in $\{[(CuL2\text{-}Me)(CuH_{-1}L2\text{-}Me)I]\cdot[(CuL2\text{-}Me)(CuH_{-1}L2\text{-}Me)]I_3\}(I_2)(I_5)_3(I_7)$ (3) and $[(CuL2\text{-}Me_3)(CuH_{-1}L2\text{-}Me_3)I](I_2)_2(I_5)_2$ (4)

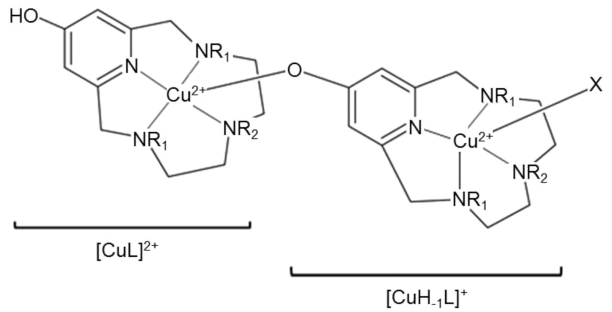

The resulting formula of the crystalline compounds are $\{[(CuL2\text{-}Me)(CuH_{-1}L2\text{-}Me)I]\cdot[(CuL2\text{-}Me)(CuH_{-1}L2\text{-}Me)]I_3\}(I_2)(I_5)_3(I_7)$ (**3**) and $[(CuL2\text{-}Me_3)(CuH_{-1}L2\text{-}Me_3)I](I_2)_2(I_5)_2$ (**4**)). Drawings of the dinuclear cations are shown in Figure 8. Details of coordination geometry (bond distances and angles) are reported in Tables S5 and S6, while bond distances and angles for iodine molecules and polyiodide anions are listed in Tables S7 and S8.

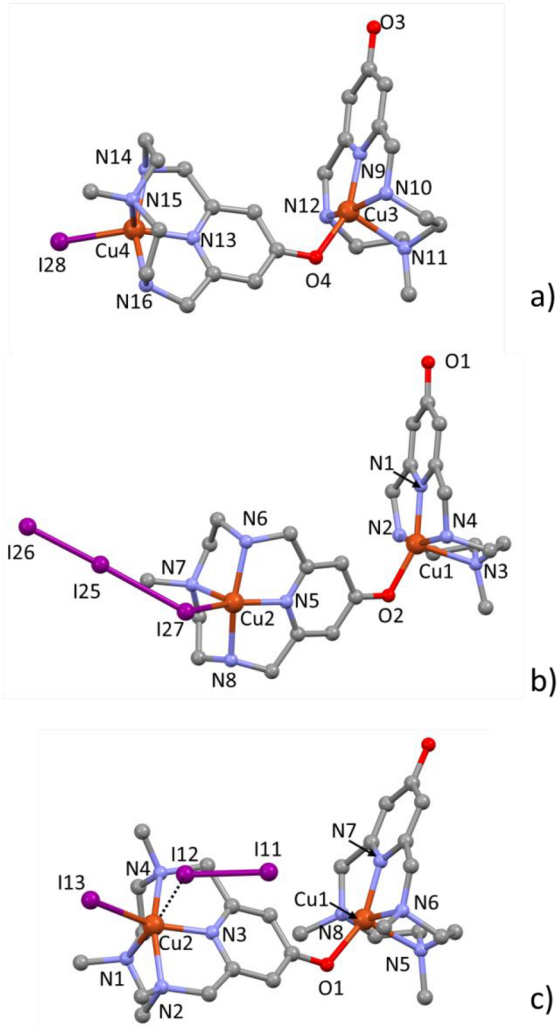

Figure 8. Crystal structures of the $[(CuL2\text{-}Me)(CuH_{-1}L2\text{-}Me)X]^{2+}$ dinuclear cations in compound **3**, X = I^- (a) or X = I_3^- (b), and of the $[(CuL2\text{-}Me_3)(CuH_{-1}L2\text{-}Me_3)I]^{2+}$ dinuclear cations in compound **4** (c); Cu2−I13 2.555(3), Cu2···I12 3.306(4) Å, Cu2···I11 5.324(4) Å.

As observed in the previous structures, also in these complexes, the ligands assume the *cis*-folded N_4 configuration. In each $(CuL)^{2+}$ unit (L = **L2-Me**, **L2-Me$_3$**), the copper ion is coordinated by the four macrocyclic nitrogen atoms and by the pyridinol oxygen from the $(CuH_{-1}L)^+$ unit, while in each $(CuH_{-1}L)^+$ unit, the coordination sphere includes the four macrocyclic nitrogen atoms and an exogenous species which can be a monatomic iodide or a triiodide anion. With only one exception (see description of compound **3**), the coordination geometries are square pyramidal: the nitrogen atom across from the pyridinol group occupies the apical position, while the remaining three nitrogen atoms define the basal plane together with the pyridinol oxygen (in $(CuL)^{2+}$) or the exogenous ligand (in $(CuH_{-1}L)^+$). In **4**, an iodine atom from an I_2 molecule occupies, at very long distance (Cu2···I12 3.306(4) Å), the sixth position of a distorted octahedron. A similar copper coordinated I_2 molecule, featuring Cu−I distance significantly shorter than the sum of the van der Waals radii, was previously reported by Hu et al.[82] Analogously to compounds **1** and **2**, the two copper units in each

https://doi.org/10.1021/acs.inorgchem.1c02967
Inorg. Chem. 2022, 61, 368−383

$[(CuL)(CuH_{-1}L)X]^{2+}$ dinuclear cation are rotated, with respect to each other, with dihedral angles of 81.3° (X = I^-) and 74.2° (X = I_3^-) in **3** and 81.4° in **4** (as measured by the angle between the mean planes of pyridine rings).

The asymmetric unit of **3** contains two $[(Cu\mathbf{L2\text{-}Me})(CuH_{-1}\mathbf{L2\text{-}Me})X]^{2+}$ binuclear complexes which differ in X, this being I^- in one case and an end-on coordinated I_3^- anion in the other (Figure 8a,b). The I^- is disordered and spread over two positions, which account for the 65% (I28) and the 35% (I29) of the overall iodide electron density. All figures, tables, and discussions reported here refer only to the most populated I28 (see Figure S8 for the I29 minor component). The coordination sphere of the $(CuH_{-1}\mathbf{L2\text{-}Me})I$ unit (Figure 8a), which represents the exception mentioned above, can be best described as a distorted trigonal bipyramid having the iodide, the pyridine N13 and the methylated N15 nitrogen atoms in the equatorial plane, and the two benzylic nitrogen atoms in the apical positions. Both $[(Cu\mathbf{L2\text{-}Me})(CuH_{-1}\mathbf{L2\text{-}Me})X]^{2+}$ (X = I^-, I_3^-) interact with their own copies translated along the *b* axis (Figure 9), giving rise to rather strong[83] charge

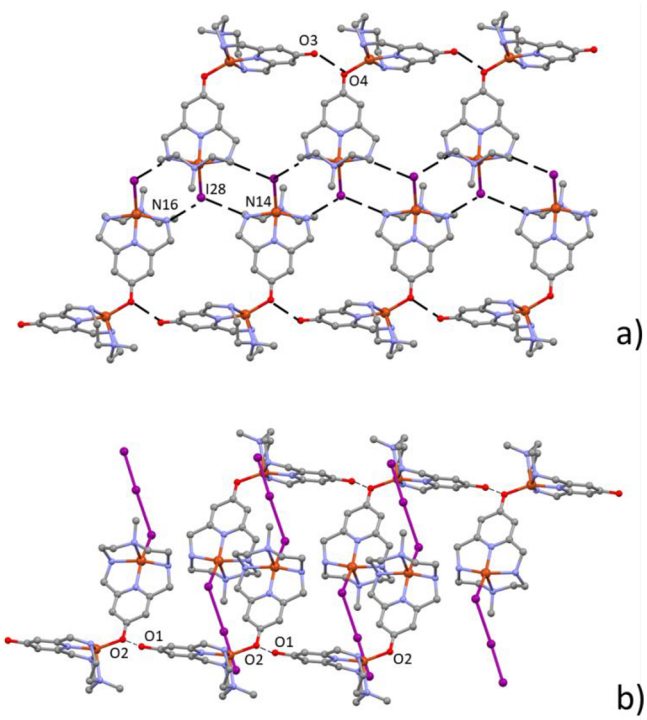

Figure 9. Compound **3**. (a) Array, growing along the *b* axis, of $[(Cu\mathbf{L2\text{-}Me})(CuH_{-1}\mathbf{L2\text{-}Me})I]^{2+}$ binuclear complexes linked by charge assisted OH···O^- and NH···I^- H-bonds. (b) Array, growing along the *b* axis, of $[(Cu\mathbf{L2\text{-}Me})(CuH_{-1}\mathbf{L2\text{-}Me})I_3]^{2+}$ binuclear complexes linked by charge assisted OH···O^- H-bonds.

assisted OH···O^- H-bonds involving their protonated and deprotonated pyridinol oxygen atoms (2.59(1) Å for O1···$O2^-$ in $[(Cu\mathbf{L2\text{-}Me})(CuH_{-1}\mathbf{L2\text{-}Me})I_3]^{2+}$ and 2.60(1) Å for O3···$O4^-$ in $[(Cu\mathbf{L2\text{-}Me})(CuH_{-1}\mathbf{L2\text{-}Me})I]^{2+}$). In $[(Cu\mathbf{L2\text{-}Me})(CuH_{-1}\mathbf{L2\text{-}Me})I]^{2+}$, adjacent cations form additional NH···I^- H-bonds with the coordinated I28 anions (Figure 9a, N16···I28, 3.53(1) Å; N14···I28, 3.61(1) Å). By this way, chains of equivalent binuclear complexes develop along the *b* axis, which are completely surrounded by an intricate network of polyiodide anions and iodine molecules. Several I···I contacts are very short and can be described as secondary bonds, being below the accepted threshold of 3.7 Å.[37] Some of them (I1···I3, 3.388(2) Å; I11···I23, 3.384(1) Å) are just above the boundary between intra- and intermolecular distances (3.3 Å).[84] These networks are shown in Figure 10, while Table 4

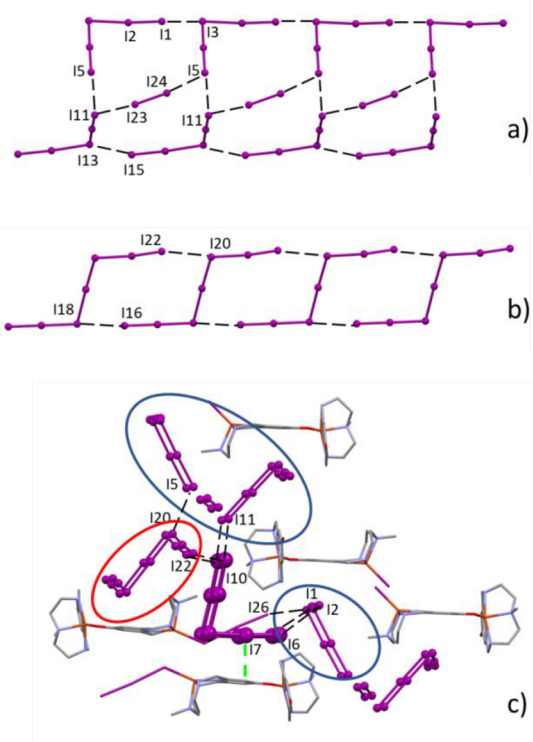

Figure 10. Compound **3**. Tapes of (I_5^- + I_2)-based 11-atom rings (a) and I_7^--based 10-atom rings (b) joined by secondary I···I bonds. Details for the crystal packing evidencing the pentaiodide anions connecting the I_7^--based 10-atom rings (red circle) and the (I_5^- + I_2)-based 11-atom rings (blue circles) (c). Anion−π interaction marked by a green dashed line.

Table 4. Selected Contacts (Å) Involving Iodine Atoms in Compound 3

N14···I28	3.61(1)	I15···I13	3.733(2)
N16···I28	3.53(1)	I22···I10	3.755(1)
I1···I3	3.388(2)	I11···I5	3.798(1)
I11···I23	3.384(1)	I1···I26	3.821(2)
I5···I24	3.500(2)	I2···I6	3.850(2)
I10···I11	3.567(1)	I16···I18	3.886(1)
		I5···I20	3.935(2)

lists relevant I···I contacts. The chains formed by the $[(Cu\mathbf{L2\text{-}Me})(CuH_{-1}\mathbf{L2\text{-}Me})I]^{2+}$ cations are surrounded by polyiodide anions and iodine molecules arranged in ribbons of 11-atom rings (Figure 10a), while in the case of $[(Cu\mathbf{L2\text{-}Me})(CuH_{-1}\mathbf{L2\text{-}Me})I_3]^{2+}$ chains, the array of metal complexes is surrounded by I_7^- anions which generate tapes of 10-atom rings (Figure 10b).

Analyses of the shortest I···I contacts in the crystal packing evidence the role of an additional pentaiodide anion, which connects the I_7^--based 10-atom rings with the 11-atom rings based on I_5^- + I_2. Notably, the latter 11-atom rings are also in direct contact with the coordinated triiodide of $[(Cu\mathbf{L2\text{-}Me})(CuH_{-1}\mathbf{L2\text{-}Me})I_3]^{2+}$ (I1···I26, 3.821(2) Å) (Figure 10c).

https://doi.org/10.1021/acs.inorgchem.1c02967
Inorg. Chem. 2022, 61, 368−383

This gluing pentaiodide anion gives a very short anion-π contact with the pyridinol ring in $(CuH_{-1}$**L2-Me**$)]I_3$ (I7···ring centroid, 3.6 Å; Figure 10c). A strong anion−π interaction also involves the pyridinol ring of $(CuH_{-1}$**L2-Me**$)I$ and one of its surrounding pentaiodide (I3···ring centroid, 3.6 Å; Figure S9). As shown below, the involvement of the pyridinol group in two coordination bonds (through the pyridine nitrogen and the deprotonated pyridinol oxygen), established by both $(CuH_{-1}$**L2-Me**$)I_3$ and $(CuH_{-1}$**L2-Me**$)I$ units, greatly depletes the aromatic ring of its electron density, so providing an important and peculiar anchor point for polyiodide binding.

The crystal structure of $[(Cu$**L2-Me$_3$**$)(CuH_{-1}$**L2-Me$_3$**$)I]$-$(I_2)_2(I_5)_2$ (**4**) shows strong similarity with the structures of compound **3**. Despite the presence of an iodine molecule occupying the sixth position of a distorted octahedron (Figure 8c), the $[(Cu$**L2-Me$_3$**$)(CuH_{-1}$**L2-Me$_3$**$)I]^{2+}$ dinuclear cations form chains developing along the *b* axis, where protonated and deprotonated pyridinol oxygen atoms from neighboring units give strong OH···O$^-$ H-bonds (Figure 11a).

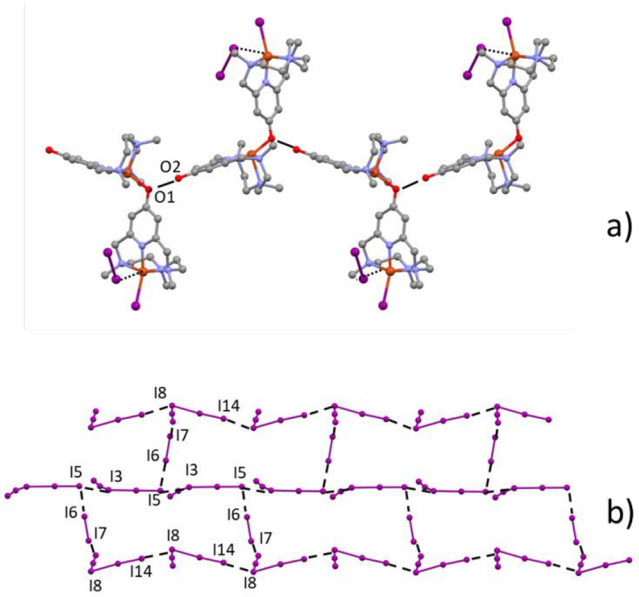

Figure 11. Compound **4**. Array, growing along the *b* axis, of $[(LCu)(LH_{-1}Cu)I]^{2+}$ binuclear complexes linked by charge assisted OH···O$^-$ H-bonds. Iodine molecules, occupying the sixth coordination position of a distorted octahedron around Cu1, are also shown (a). 18-membered rings based on iodine molecules and pentaiodide anions (b).

The remaining not coordinated iodine molecules and the pentaiodide anions form I···I secondary bonds which define the 2D grid shown in Figure 11b (selected I···I distances are listed in Table 5). The grid meshes, constituted by 18-atom rings, are in contact with the coordinated iodine molecules giving iodine−iodine contacts which are well below the iodine−iodine secondary bond threshold (I3···I11 and I12···I13 distances 3.476(3) and 3.361(3) Å, respectively, Figure S10). A few longer I···I contacts contribute to the overall stabilization of the crystal packing (Table 5 and Figure S10).

Table 5. Selected Contacts (Å) Involving Iodine Atoms in Compound 4

I3···I5	3.365(3)	I8···I14	3.560(2)
I12···I13	3.361(3)	I1···I7	3.738(3)
I5···I6	3.430(2)	I1···I8	3.945(2)
I7···I8	3.466(2)	I11···I10	3.938(3)
I3···I11	3.476(3)		

Considerations on the Crystal Structures: Hirshfeld Surface Analysis and I···I Contacts Details. Percentage composition of Hirshfeld surfaces,[63−65] in terms of atoms in contact, is found very similar among the units $[(Cu$**L2-Me**$)(CuH_{-1}$**L2-Me**$)I]^{2+}$, formally coordinated by I_3^-, $[(Cu$**L2-Me**$)(CuH_{-1}$**L2-Me**$)I]^{2+}$, formally coordinated by I^-, and $[(Cu$**L2-Me$_3$**$)(CuH_{-1}$**L2-Me$_3$**$)I]^{2+}$ (Figure S11, Table S9), as expected for similar molecules surrounded by polyiodides networks.

Far more insights can be obtained from comparison of the related fingerprint plots (Figure 12). The most prominent shared feature among fingerprint plots of these **L2** derivatives is the appearance of two O···H tips typical of strong and

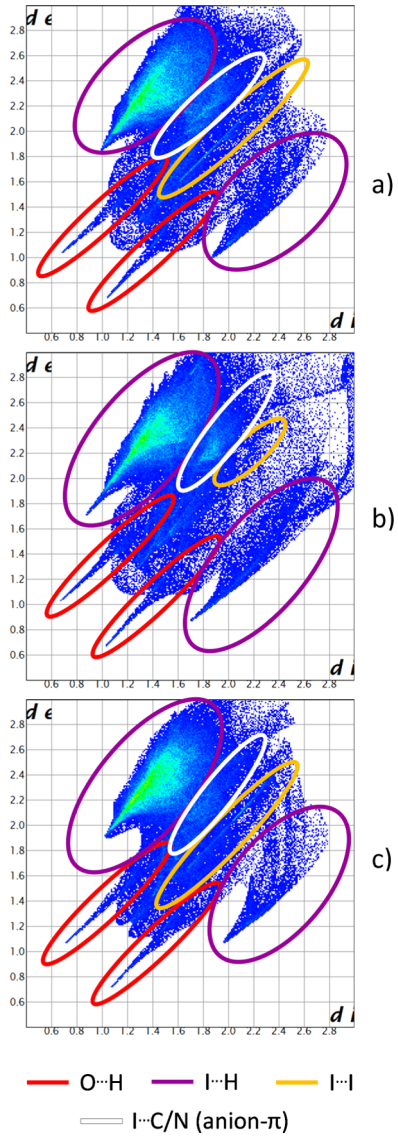

Figure 12. Global fingerprint plots for: **3**, surface of $[(CuL)(CuH_{-1}L)I]^{2+}$ formally coordinated by I_3^- (a); **3**, surface of $[(CuL)(CuH_{-1}L)I]^{2+}$ formally coordinated by I^- (b); **4**, surface of $[(CuL)(CuH_{-1}L)I]^{2+}$ (c). For plots related to individual types of contact, see Figure S11.

https://doi.org/10.1021/acs.inorgchem.1c02967
Inorg. Chem. 2022, 61, 368−383

directional H-bonding (Figure 12, red circles). Of course, O···H contacts were absent in **L1**-based structures (they do not have an −OH function). On the contrary, H···I type contacts (Figure 12, purple circles) pass relatively unmodified from **L1**- to **L2**-based structures.

In the case of **L-Me** (**L** = **L1**, **L2**), the $[(Cu\mathbf{L\text{-}Me})I]^+$ tectons organize themselves in ribbons held together by long NH···I interactions involving the coordinated iodide anion (Figures 9 and 13). The subtending network adapts from the relatively unconstrained situation found in the **L1-Me** complex (shortest NH···I distances, Figure 13a), to the more hindered situation of **L2-Me** (Figure 13b), where additional space is required to accommodate the dinuclear complex, to the crowded situation generated by the presence of coordinated I_3^- (Figure 13c), where making room for the protruding I_3^- requires involvement of further polyiodides (I_5^-) to keep the chain in place, thus increasing the spacing within complexes in the ribbon. As a matter of fact, the two types of H-bond donor−acceptor pairs, that is, NH···I and OH···O, do never mix up.

C···I and N···I contacts (Figure 12, white circles), mostly related to anion-π type interactions,[28,30,85,86] are significantly more developed for **L2**-based structures than for **L1**-based ones. Given the pivotal role of ring electrostatic potential/polarization,[28,87−91] the more relevant role of these interactions is most likely due to the superior polarization of the aromatic portion of **L2** derivatives, especially when both amino and phenolic functions coordinate to Cu(II).

Coming to polyiodides and I···I contacts (Figure 12, yellow circles, and Figure S12d), it is relatively clear—notice the tip that shows the mutual piercing of interacting partners into one another electronic density—that the difference between Cu−I···I_2 in **3** (Figure S12d, left column), which we interpreted as a Cu-bound I_3^-, and I^-···I_2 distance in Cu(II) coordination sphere in **4** (Figure S12d, right column), which we interpreted as individual I^-···I_2 entities, is rather tiny, while it is enormous with respect to polyiodides merely touching themselves (Figure S12d, central column). A real discrimination between fully covalent and fully supramolecular contacts can hardly happen in the spatial region that goes from 3.1 to 3.4 Å (Figure 14). As discussed elsewhere,[36,37] variability of I−I covalent bonds is already large for triiodides. A Lorentzian curve centered at 2.9179(1) Å and possessing a full width at half-maximum of 0.0436(3) Å (R^2 = 0.997, χ^2 = 13.27) best describes I_3^- experimental bond lengths. Accordingly, bond lengths ≥3.1 Å are already quite odd for triiodide, as they already fall well above the center + 3 fwhm level. The "Gaussian" tends to get smeared further already for pentaiodides (for I_5^- mean distal I−I bond length ±1 standard

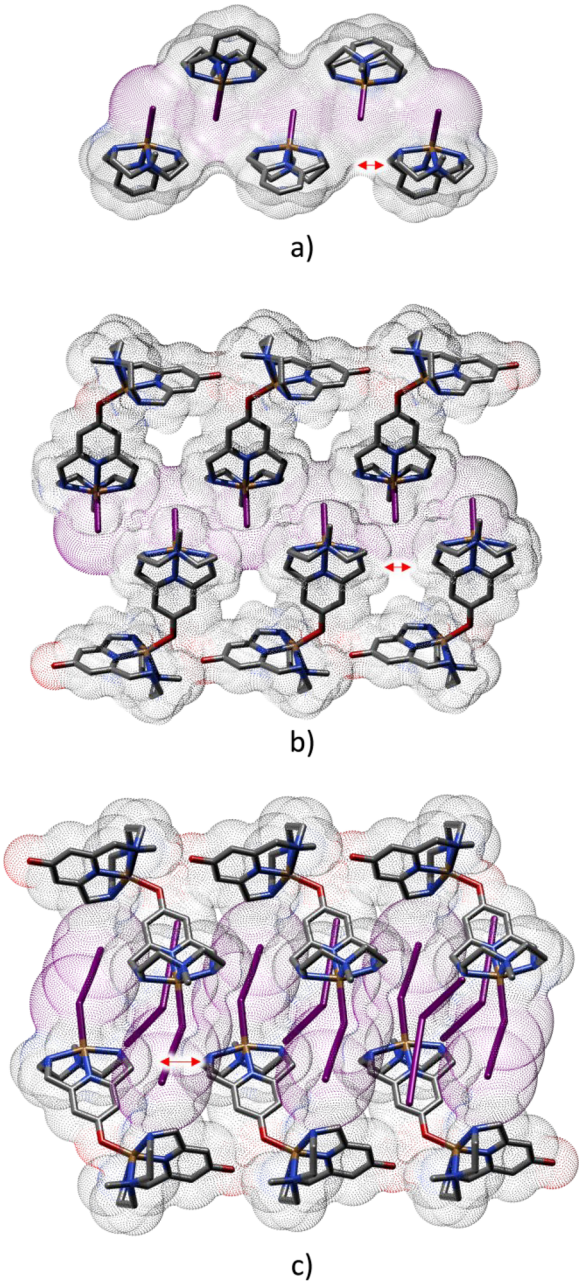

Figure 13. NH···I H-bonded ribbons as found in **L1-Me**-based crystals[30] (a) and in **3** (coordinated I^-, (b) and I_3^-, (c), respectively).

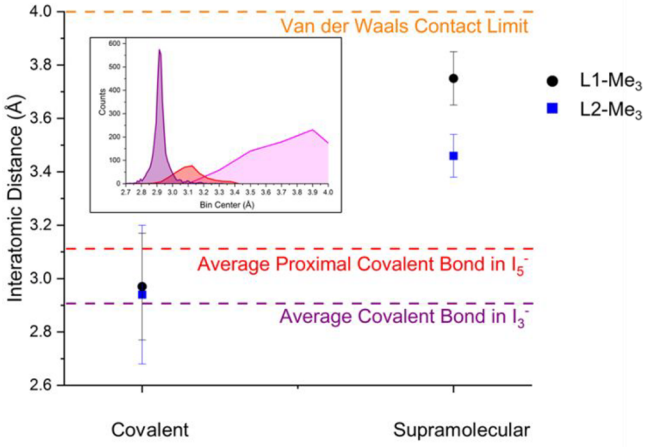

Figure 14. Comparison of I−I covalent and supramolecular distances as found in **L1-Me$_3$**- and **L2-Me$_3$**-containing crystalline phases (average value, standard deviation as error bar). Relevant reference distances (average I−I bond length in I_3^-, proximal covalent bond in I_5^- and van der Waals contact distance) are also reported to scale for comparison purposes. Inset shows (left to right) covalent bond distribution for I_3^- (violet) and interaction distances of I_3^- subunits with generic I_2 probes, either covalent (i.e., pentaiodide proximal bond distances, red) or supramolecular (pink), in order to give an appropriate view of actual broadness of statistical distributions. Reproduced with permission from ref 36. Copyright 2021 Royal Society of Chemistry.

https://doi.org/10.1021/acs.inorgchem.1c02967
Inorg. Chem. 2022, 61, 368−383

deviation is 2.80 ± 0.04 Å, while the proximal one is 3.1 ± 0.1 Å, Figure 14).

Cu(II)-coordinated triiodide in **3** and Cu(II)-coordinated I_2 in **4** are clearly borderline cases. In the latter, the I_2 molecule is virtually equidistant from Cu(II) (3.305 Å) and coordinated I^- (3.361 Å) (i.e., with respect to sum of the ionic or van der Waals radii, I···I interaction should be stronger than I···Cu), being coordinated at rather unusual angles with respect to both the metal center (I−I−Cu angle of 122.7°, i.e. significantly larger than tetrahedral) and the coordinated I^- (I−I···I^- angle of 165.9°, i.e. significantly smaller than 180°).

We commented above the similarity of Cu(II) complexes with **L1-Me** and **L2-Me** in giving H-bonded ribbons. It is now interesting to extend such comparison to polyiodide complexes produced by Cu(II) complexes of **L1-Me$_3$** and **L2-Me$_3$**. As observed before, complete removal of H-bond donors by methylation led to crystal structures whose directionality is dominated by I···I interactions. In the case of [Cu(**L1-Me$_3$**)I]$^+$, this led to strong interaction with an I_2 molecule (assigned as coordinated I_3^-, Cu−I···I_2 distance of 3.244 Å, same distance is 3.237 in **3**, cf. above discussion) and catenation with pentaiodides in forming 11-membered polyiodide rings fused in a chain. The covalent (2.97 ± 0.21 Å) and supramolecular (3.75 ± 0.01 Å) nature of the interactions within said rings remained quite manifest from interatomic distances (Figure 14).

The situation in **4** is hardly comparable, most likely because of the constraints imposed by OH···O interactions (apparently indifferent to the degree of N-methylation) and bulkiness of the dinuclear complexes. Notwithstanding such intrinsic differences, an 18-atom tile (Figure 11b) is clearly distinguishable as the main repeating pattern. Within such a grid, we observe that average length of covalent bonds is not significantly different from above **L1-Me$_3$** data, but the distinction between covalent bonds (in **4**, 2.94 ± 0.26) and supramolecular contacts (in **4**, 3.46 ± 0.08) is now significantly reduced (Figure 14).

This observation cannot be *tout court* ascribed to iodine density, which is slightly lower for **4** than for [Cu(**L1-Me$_3$**)(I·I_2)](I_5)[30] (I_N = 0.443 for **4** vs 0.472 for the latter),[49] nor it is easily justified by simply counting charges per ring, seeking to prove a lessened electrostatic repulsion among polyiodides: In order to do so, one should postulate to know where charges are localized in the first place. This is in direct conflict with the (sounder) idea that intraring supramolecular bond lengths in **4** are significantly shortened because of partial charge transfer. If such is indeed the case, we can conclude that with **L2-Me$_3$**, relative to **L1-Me$_3$**, we come much closer to a real polyiodide network that can be hardly considered as discrete anions due to their strong mutual interactions.

Electronic Spectra. The UV−vis spectrum of the Cu(II) complex with **L2**, obtained in aqueous solution at pH 6, had already been reported.[48] It consists of an intense $\pi \rightarrow \pi^*$ charge-transfer band at 249 nm with a shoulder in the 284−330 nm region, typical of the ligand, and a very weak and broad d−d band around 699 nm. We have now recorded the spectra of the Cu(II) complexes with the three pyridinol ligands considered here, in the 200−800 nm region and under pH conditions corresponding to about 100% formation of the (CuH$_{-1}$L)$^+$ (L = **L2**, **L2-M2**, **L2-Me$_3$**) species. In the UV region (Figure S13), all three complexes show charge-transfer bands at 248−251 nm, with a shoulder in the 260−275 nm region, which are practically coincident, though somewhat more intense and slightly blue-shifted, with those recorded for the uncomplexed ligands in the same pH conditions (Figure S14). Another smoother and weaker band is clearly visible at about 305 nm in the spectrum of (CuH$_{-1}$**L2-Me$_3$**)$^+$ that becomes less evident in the spectra of the other two complexes. Very strong ligand-centered transitions (not characterized) are present below 220 nm (Figure S13).

The visible region of these spectra is characterized by broad and weak d−d bands centered around 680 nm [(CuH$_{-1}$**L2**)$^+$], 682 nm [(CuH$_{-1}$**L2-Me**)$^+$], and 656 nm [(CuH$_{-1}$**L2-Me$_3$**)$^+$] that are responsible for the blue color of the complexes (Figure S13).

In the electronic spectra of the solid polyiodide complexes **3** and **4**, the bands of the complexes below 400 nm overlap the bands of the polyiodide anions. The strong ligand-centered transition below 220 nm is still present, while two bands at 301/305 nm and 400/411 nm characterize the spectra of **4**/**3** (Figure S15). These bands are consistent with the presence of I_{2n+1}^- (n = 1−3) anions and are located at relatively low energies, especially the 400/411 nm ones, in agreement with the content of I_5^- and I_7^- anions.[37] Tails of the 400/411 nm bands extend toward longer wavelengths in accordance with the presence of lower energy absorption components expected for polyiodides higher than I_3^-, which are more clearly evidenced by the shoulder emerging at about 600 nm in the spectrum of **4**.

■ CONCLUSIONS

As expected, the presence of the ionizable hydroxyl group on the pyridine ring led to the involvement of the pyridinol group in the coordination to two metal ions. This does not occur in solution, where only Cu(II) complexes with 1:1 metal:ligand stoichiometry are formed, while, in the solid state, bridging coordination of the hydroxyl group gives rise to polymeric coordination chains of general formula $\{[Cu(H_{-1}L)]\}_n^{n+}$ (L = **L2-Me**, **L2-Me$_3$**). The presence in solution of the I^-/I_2 couple induces crystallization of compounds in which this polymerization tendency stops with the formation of [(CuL)-(CuH$_{-1}$L)]$^{3+}$ (L = **L2-Me**, **L2-Me$_3$**) dimers that are surrounded by polyiodide networks.

While these new features become immediately evident in the comparison between **L1**- and **L2**-based ligands, the understanding of how these structural changes correlate with the formation of different polyiodide networks appears to be challenging, especially because of the large structural difference between the involved cations, which are monomeric complexes, in the case of **L1**-based ligands, and dimeric complexes in the case of the **L2**-based analogues. Nevertheless, this challenging task is central to the main goal of this work, that is, the understanding of how covalent, coordination, and supramolecular forces can be used, mixed together, to construct robust polyiodide networks extending across the crystals, bearing in mind the applicative opportunity of using these compounds as solid-state conductors.

First of all, we can highlight a common feature of the two series of ligands: For both of them, the formation of polyiodide networks appears to be dominated by H-bonds until full ligand N-methylation is achieved, then, I···I interactions become the main directional forces. That is, N-methylation can be helpfully used to gradually shift the directional control of the assembly process from H-bonds, mainly involving complex units, to I···I interactions, mainly involving iodine-based units.

https://doi.org/10.1021/acs.inorgchem.1c02967
Inorg. Chem. 2022, 61, 368−383

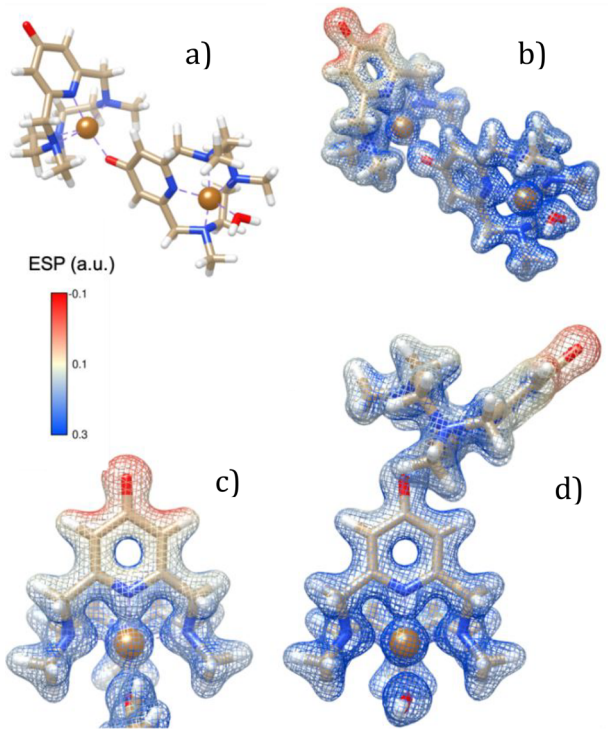

Figure 15. Representation of the ESP maps of $[(Cu\mathbf{L2}\text{-}\mathbf{Me}_3)(CuH_{-1}\mathbf{L2}\text{-}\mathbf{Me}_3)I]^{2+}$. (a) Representation of the dimeric complex. (b) Representation of the ESP map of the dimeric complex, overlaid to the representation of its structure. (c) Detail of the ESP map of the pyridinol ring in which the oxygen atom is not interacting with a copper atom. (d) Detail of the ESP map of the pyridinol ring in which the oxygen atom is bonded to the copper atom of the second complex.

Nevertheless, hydrogen bonding by the pyridinol −OH group, which is indifferent to the degree of N-methylation of the ligands, determines the formation of complex chains functioning as molds for the construction of polyiodide ribbons (constituted by 10- and 11-atom rings in **3** and by 18-atom rings in **4**) that run parallel to the complex chains and interact with them via I···I interactions, involving metal-coordinated iodine atoms (I_3^- in **3** and I_2 in **4**), and short anion−π contacts.

With respect to the latter, anion−π interactions appear to be significantly more developed for **L2**-based structures than for **L1**-based ones, thanks to the deprotonated pyridinol groups involved in O- and N-coordination to Cu(II) ions. It is known that azines may act as π-acid ligands, which can bind anions above their centers according to their positive ESPs and their molecular quadrupole moments.[28] Indeed, *s*-tetrazine, the most polarized molecule of this family (Q_{zz} quadrupole moment of 11.4 Buckinghams), is prodigal in forming anion−π interactions,[89] even in solution, as recently shown by some of us.[89,92−97] Nonetheless, also pyridine, despite being the less polarized azine (Q_{zz} quadrupole moment of 3.0 Buckinghams), forms anion−π complexes,[28] especially when they are activated by electron-withdrawing substituents[98] or by N-interaction with positive charges (H^+, metal ions).[99,100] Insertion of an electron-donating −OH group on the pyridine rings is expected to hinder anion−π interactions, but deprotonation of this hydroxyl function and coordination to metal ions of both O and N donors of the pyridinol group, like in our complexes, turns the negatively charged surface of the ring into a markedly positive surface (Figure 15) capable of attracting anions.

Finally, it is worth noting that supramolecular I···I interactions are shorter in **L2**-based polyiodides, relative to **L1**-based ones, despite the fact that the iodine density (iodine number I_N = 0.454 for **3** and I_N = 0.443 for **4**) does not follow the same trend, due to the bulkier dimeric complex cations. Especially in the case of **4**, such shortening of the I···I contacts considerably blurs the identity of the individual iodine-based components in favor of iodine networks in which the orbital overlap, essential for the Grotthuss-type conduction mechanism,[37,38] gains importance.

■ ASSOCIATED CONTENT

Supporting Information

The Supporting Information is available free of charge at https://pubs.acs.org/doi/10.1021/acs.inorgchem.1c02967.

Distribution diagrams, tables of crystallographic bond distances and angles, Hirshfeld surface compositions and plots, crystal data and refinement, additional views of the crystal structures, ^{1}H NMR and UV−vis spectra (PDF)

Accession Codes

CCDC 2062421−2062422 and 2094997−2094998 contain the supplementary crystallographic data for this paper. These data can be obtained free of charge via www.ccdc.cam.ac.uk/data_request/cif, or by emailing data_request@ccdc.cam.ac.uk, or by contacting The Cambridge Crystallographic Data Centre, 12 Union Road, Cambridge CB2 1EZ, UK; fax: +44 1223 336033.

■ AUTHOR INFORMATION

Corresponding Authors

Antonio Bianchi − *Department of Chemistry "Ugo Schiff", University of Florence, 50019 Sesto Fiorentino, Italy;* orcid.org/0000-0002-1082-3911; Email: antonio.bianchi@unifi.it

Enrique García-España − *ICMol, Department of Inorganic Chemistry, University of Valencia, 46980 Paterna, Spain;* orcid.org/0000-0002-4601-6505; Email: enrique.garcia-es@uv.es

Authors

Álvaro Martínez-Camarena − *ICMol, Department of Inorganic Chemistry, University of Valencia, 46980 Paterna, Spain;* orcid.org/0000-0001-9910-6961

Matteo Savastano − *Department of Chemistry "Ugo Schiff", University of Florence, 50019 Sesto Fiorentino, Italy;* orcid.org/0000-0002-9780-7542

Salvador Blasco − *ICMol, Department of Inorganic Chemistry, University of Valencia, 46980 Paterna, Spain;* orcid.org/0000-0002-8142-8337

Estefanía Delgado-Pinar − *ICMol, Department of Inorganic Chemistry, University of Valencia, 46980 Paterna, Spain; Department of Chemistry, CQC, University of Coimbra, P3004-535 Coimbra, Portugal;* orcid.org/0000-0002-7400-5715

Claudia Giorgi − *Department of Chemistry "Ugo Schiff", University of Florence, 50019 Sesto Fiorentino, Italy*

Carla Bazzicalupi − *Department of Chemistry "Ugo Schiff", University of Florence, 50019 Sesto Fiorentino, Italy;* orcid.org/0000-0003-4602-0405

Complete contact information is available at:

https://pubs.acs.org/10.1021/acs.inorgchem.1c02967

Author Contributions

[‖]These authors contributed equally.

Notes

The authors declare no competing financial interest.

■ ACKNOWLEDGMENTS

This work was supported by the Spanish Ministry of Science, Innovation and Universities-FEDER (PID2019-110751RB-I00, RED2018-102331-T, Unidad de Excelencia María de Maeztu CEX2019-000919-N, FPU14/05098 and EST17/00666). This contribution is also based upon work from COST Action CA18202, NECTAR - Network for Equilibria and Chemical Thermodynamics Advanced Research, supported by COST (European Cooperation in Science and Technology).

■ REFERENCES

(1) Bianchi, A.; García-España, E. Azacycloalkanes and Azacyclophanes. In *Supramolecular Chemistry: From Molecules to Nanomaterials*; Gale, P. A., Steed, J. W., Eds.; John Wiley & Sons: Chichester, 2012; pp 753−784.

(2) Stetter, H.; Frank, W.; Mertens, R. Darstellung und komplexbildung von polyazacycloalkan-N-essigsäuren. *Tetrahedron* **1981**, *37*, 767−772.

(3) Frías, J. C.; Soriano, J.; Blasco, S.; García-España, E.; Rodríguez-Rodríguez, A.; Esteban-Gomez, D.; Carniato, F.; Botta, M.; Platas-Iglesias, C.; Albelda, M. T. Macrocyclic pyclen-based Gd^{3+} complex with high relaxivity and pH response. *Inorg. Chem.* **2020**, *59*, 7306−7317.

(4) Tircso, G.; Kovacs, Z.; Sherry, A. D. Equilibrium and Formation/Dissociation Kinetics of Some LnIIIPCTA Complexes. *Inorg. Chem.* **2006**, *45*, 9269−9280.

(5) Pradhan, R. N.; Chakraborty, S.; Bharti, P.; Kumar, J.; Ghosh, A.; Singh, A. K. Seven coordinate Co(II) and six coordinate Ni(II) complexes of an aromatic macrocyclic triamide ligand as paraCEST agents for MRI. *Dalton Trans.* **2019**, *48*, 8899−8910.

(6) Rojas-Quijano, F. A.; Benyó, E. B.; Tircsó, G.; Kálmán, F. K.; Baranyai, Z.; Aime, S.; Sherry, D. A.; Kovács, Z. Lanthanide(III) complexes of tris(amide) PCTA derivatives as potential bimodal magnetic resonance and optical imaging agents. *Chem.—Eur. J.* **2009**, *15*, 13188−13200.

(7) Marin, C.; Inclán, M.; Ramirez-Macias, I.; Albelda, M. T.; Canas, R.; Clares, M. P.; Gonzalez-Garcia, J.; Rosales, M. J.; Urbanova, K.; Garcia-España, E.; et al. In vitro antileishmanial activity of aza-scorpiand macrocycles. Inhibition of the antioxidant enzyme iron superoxide dismutase. *RSC Adv.* **2016**, *6*, 17446−17455.

(8) Marin, C.; Clares, M. P.; Ramírez-Macías, I.; Blasco, S.; Olmo, F.; Soriano, C.; Verdejo, B.; Rosales, M. J.; Gomez-Herrera, D.; Garcia-España, E.; Sánchez-Moreno, M. In vitro activity of scorpiand-like azamacrocycle derivatives in promastigotes and intracellular amastigotes of Leishmania infantum and Leishmania braziliensis. *Eur. J. Med. Chem.* **2013**, *62*, 466−477.

(9) Olmo, F.; Marin, C.; Clares, M. P.; Blasco, S.; Albelda, M. T.; Soriano, C.; Gutiérrez-Sánchez, R.; Arrebola-Vargas, F.; Garcia-España, E.; Sánchez-Moreno, M. Scorpiand-like azamacrocycles prevent the chronic establishment of Trypanosoma cruzi in a murine model. *Eur. J. Med. Chem.* **2013**, *70*, 189−198.

(10) Wen, J.-H.; Li, C.-Y.; Geng, Z.-R.; Ma, X.-Y.; Wang, Z.-L. A potent antitumor Zn^{2+} tetraazamacrocycle complex targeting DNA: The fluorescent recognition, interaction and apoptosis studies. *Chem. Commun.* **2011**, *47*, 11330−11332.

(11) Le Fur, M.; Beyler, M.; Molnar, E.; Fougere, O.; Esteban-Gomez, D.; Tircso, G.; Platas-Iglesias, C.; Lepareur, N.; Rousseaux, N.; Tripier, R. Stable and inert Yttrium(III) complexes with pyclen-based ligands bearing pendant picolinate arms: Toward new pharmaceuticals for β-Radiotherapy. *Inorg. Chem.* **2018**, *57*, 2051−2063.

(12) Le Fur, M.; Beyler, M.; Molnar, E.; Fougere, O.; Esteban-Gomez, D.; Tircso, G.; Platas-Iglesias, C.; Lepareur, N.; Rousseaux, N.; Tripier, R. The role of the capping bond effect on pyclen $natY^{3+}/^{90}Y^{3+}$ chelates: Full control of the regiospecific N-functionalization makes the difference. *Chem. Commun.* **2017**, *53*, 9534−9537.

(13) Guijarro, L.; Inclán, M.; Pitarch-Jarque, J.; Doménech-Carbó, A.; Chicote, J. U.; Trefler, S.; García-España, E.; García-España, A.; Verdejo, B. Homo- and heterobinuclear Cu^{2+} and Zn^{2+} complexes of ditopic aza scorpiand ligands as superoxide dismutase mimics. *Inorg. Chem.* **2017**, *56*, 13748−13758.

(14) Serena, C.; Calvo, E.; Clares, M. P.; Diaz, M. L.; Chicote, J. U.; Beltrán-Debon, R.; Fontova, R.; Rodriguez, A.; García-España, E.; García-España, A. Significant in-vivo anti-inflammatory activity of Pytren4Q-Mn a superoxide dismutase 2 (SOD2) mimetic scorpiand-like Mn (II) complex. *PLoS One* **2015**, *10*, e0119102.

(15) Lincoln, K. M.; Richardson, T. E.; Rutter, L.; Gonzalez, P.; Simpkins, J. W.; Green, K. N. An N-heterocyclic amine chelate capable of antioxidant capacity and amyloid disaggregation. *ACS Chem. Neurosci.* **2012**, *3*, 919−927.

(16) Martínez-Camarena, Á.; Liberato, A.; Delgado-Pinar, E. G.; Algarra, A.; Pitarch-Jarque, J.; Llinares, J. M.; Mañez, M. Á.; Domenech-Carbó, A.; Basallote, M. G.; García-España, E. Coordination chemistry of Cu^{2+} complexes of small N-alkylated tetraazacyclophanes with SOD activity. *Inorg. Chem.* **2018**, *57*, 10961−10973.

(17) Green, K. N.; Pota, K.; Tircsó, G.; Gogolák, R. A.; Kinsinger, O.; Davda, C.; Blain, K.; Brewer, S. M.; Gonzalez, P.; Johnston, H. M.; Akkaraju, G. Dialing in on pharmacological features for therapeutic antioxidant small molecule. *Dalton Trans.* **2019**, *48*, 12430−12439.

(18) Savastano, M.; Arranz-Mascarós, P.; Clares, M. P.; Cuesta, R.; Godino-Salido, M. L.; Guijarro, L.; Gutiérrez-Valero, M. D.; Inclán, M.; Bianchi, A.; García-España, E.; López-Garzón, R. A new heterogeneous catalyst obtained via supramolecular decoration of graphene with a Pd^{2+} azamacrocyclic complex. *Molecules* **2019**, *24*, 2714.

(19) Passaponti, M.; Savastano, M.; Clares, M. P.; Inclán, M.; Lavacchi, A.; Bianchi, A.; García-España, E.; Innocenti, M. MWCNTs-supported Pd(II) complexes with high catalytic efficiency in oxygen reduction reaction in alkaline media. *Inorg. Chem.* **2018**, *57*, 14484−14488.

(20) Savastano, M.; Arranz-Mascarós, P.; Bazzicalupi, C.; Clares, M. P.; Godino-Salido, M. L.; Guijarro, L.; Gutiérrez-Valero, M. D.; Bianchi, A.; García-España, E.; López-Garzón, R. Polyfunctional tetraazamacrocyclic ligands: Zn(II), Cu(II) binding and formation of hybrid materials with multiwalled carbon nanotubes. *ACS Omega* **2017**, *2*, 3868−3877.

(21) Savastano, M.; Arranz-Mascarós, P.; Bazzicalupi, C.; Clares, M. P.; Godino-Salido, M. L.; Gutiérrez-Valero, M. D.; Inclán, M.; Bianchi, A.; García-España, E.; López-Garzón, R. Construction of green nanostructured heterogeneous catalysts via non-covalent surface decoration of multi-walled carbon nanotubes with Pd(II) complexes of azamacrocycles. *J. Catal.* **2017**, *353*, 239−249.

(22) Serrano-Plana, J.; Aguinaco, A.; Belda, R.; Garcia-España, E.; Basallote, M. G.; Company, A.; Costas, M. Exceedingly fast oxygen atom transfer to olefins via a catalytically competent nonheme iron species. *Angew. Chem., Int. Ed.* **2016**, *55*, 6310−6314.

(23) Wen, J.; Qin, S.; Ma, L.-F.; Dong, L.; Zhang, J.; Liu, S.-S.; Duan, Y.-S.; Chen, S.-Y.; Hu, C.-W.; Yu, X.-Q. Iron-mediated direct Suzuki-Miyaura reaction: A new method for the ortho-arylation of pyrrole and pyridine. *Org. Lett.* **2010**, *12*, 2694−2697.

(24) Wang, X.; Zhang, Z.; Ma, X.; Wen, J.; Geng, Z.; Wang, Z. Real-time fluorescence assays of alkaline phosphatase and ATP sulfurylase activities based on a novel PPi fluorescent probe. *Talanta* **2015**, *137*, 156−160.

(25) Wang, X.; Ma, X.; Yang, Z.; Zhang, Z.; Wen, J.; Geng, Z.; Wang, Z. An NBD-armed tetraaza macrocyclic lysosomal-targeted

fluorescent probe for imaging copper(II) ions. *Chem. Commun.* **2013**, *49*, 11263−11265.
(26) Wen, J.; Geng, Z.; Yin, Y.; Wang, Z. A versatile water soluble fluorescent probe for ratiometric sensing of Hg^{2+} and bovine serum albumin. *Dalton Trans.* **2011**, *40*, 9737−9745.
(27) Wen, J.; Geng, Z.; Yin, Y.; Zhang, Z.; Wang, Z. A Zn^{2+}-specific turn-on fluorescent probe for ratiometric sensing of pyrophosphate in both water and blood serum. *Dalton Trans.* **2011**, *40*, 1984−1989.
(28) Martínez-Camarena, Á.; Savastano, M.; Bazzicalupi, C.; Bianchi, A.; García-España, E. Stabilisation of Exotic Tribromide (Br_3^-) Anions via Supramolecular Interaction with A Tosylated Macrocyclic Pyridinophane. A Serendipitous Case. *Molecules* **2020**, *25*, 3155.
(29) Savastano, M.; Martínez-Camarena, Á.; Bazzicalupi, C.; Delgado-Pinar, E.; Llinares, J. M.; Mariani, P.; Verdejo, B.; García-España, E.; Bianchi, A. Stabilization of supramolecular networks of polyiodides with protonated small tetra-azacyclophanes. *Inorganics* **2019**, *7*, 48.
(30) Martínez-Camarena, Á.; Savastano, M.; Llinares, J. M.; Verdejo, B.; Bianchi, A.; García-España, E.; Bazzicalupi, C. Stabilization of polyiodide networks with Cu(II) complexes of small methylated polyazacyclophanes: shifting directional control from H-bonds to I···I interactions. *Inorg. Chem. Front.* **2020**, *7*, 4239−4255.
(31) Edis, Z.; Raheja, R.; Bloukh, S. H.; Bhandare, R. R.; Sara, H. A.; Reiss, G. J. Antimicrobial Hexaaquacopper(II) Complexes with Novel Polyiodide Chains. *Polymers* **2021**, *13*, 1005.
(32) Edis, Z.; Bloukh, S. H.; Sara, H. A.; Bhakhoa, H.; Rhyman, L.; Ramasami, P. Smart" triiodide compounds: Does halogen bonding influence antimicrobial activities? *Pathogens* **2019**, *8*, 182.
(33) Bloukh, S. H.; Edis, Z. Structure and Antimicrobial properties of bis(1,4,7,10-tetraoxacyclododecane-κ^4O,O′,O′′,O′′′)cesium pentaiodide, $C_{16}H_{32}CsI_5O_8$. *Z. Kristallogr. NCS* **2020**, *235*, 759−761.
(34) Adonin, S. A.; Sokolov, M. N.; Fedin, V. P. Polyhalide-bonded metal complexes: Structural diversity in an eclectic class of compounds. *Coord. Chem. Rev.* **2018**, *367*, 1−17.
(35) Hu, J.; Zhou, J.; Cao, S. An unusual cuprous iodide polymer incorporating I^-, I_2 and I_3^- structural units. *Dalton Trans.* **2018**, *47*, 17216−17220.
(36) Savastano, M. Words in Supramolecular Chemistry: the Ineffable Advances of Polyiodide Chemistry. *Dalton Trans.* **2021**, *50*, 1142−1165.
(37) Svensson, P. H.; Kloo, L. Synthesis, structure, and bonding in polyiodide and metal iodide-iodine systems. *Chem. Rev.* **2003**, *103*, 1649−1684.
(38) De Grotthuss, C. J. D. Sur la décomposition de l'eau et des corps qu'elle tient en dissolution à l'aide de l'électricité galvanique. *Ann. Chim.* **1806**, *58*, 54−73.
(39) Stegemann, H.; Rohde, A.; Reiche, A.; Schnittke, A.; Füllbier, H. Room temperature molten polyiodides. *Electrochim. Acta* **1992**, *37*, 379−383.
(40) Kusabayashi, S.; Mikawa, H.; Kawai, S.; Uchida, M.; Kiriyama, R. Semiconducting Properties of Organic Polyiodides. *Bull. Chem. Soc. Jpn.* **1964**, *37*, 811−817.
(41) Poręba, T.; Świątkowski, M.; Kruszyński, R. Molecular self-assembly of 1D infinite polyiodide helices in a phenanthrolinium salt. *Dalton Trans.* **2021**, *50*, 2800−2806.
(42) Pulli, E.; Rozzi, E.; Bella, F. Transparent photovoltaic technologies: Current trends towards upscaling. *Energy Convers. Manage.* **2020**, *219*, 112982.
(43) Wu, J.; Lan, Z.; Lin, J.; Huang, M.; Huang, Y.; Fan, L.; Luo, G. Electrolytes in Dye-Sensitized Solar Cells. *Chem. Rev.* **2015**, *115*, 2136−2173.
(44) Abbas, Q.; Fitzek, H.; Schröttner, H.; Dsoke, S.; Gollas, B. Immobilization of Polyiodide Redox Species in Porous Carbon for Battery-Like Electrodes in Eco-Friendly Hybrid Electrochemical Capacitors. *Nanomaterials* **2019**, *9*, 1413.
(45) Meng, Z.; Tian, H.; Zhang, S.; Yan, X.; Ying, H.; He, W.; Liang, C.; Zhang, W.; Hou, X.; Han, W.-Q. Polyiodide-Shuttle Restricting Polymer Cathode for Rechargeable Lithium/Iodine Battery with Ultralong Cycle Life. *ACS Appl. Mater. Interfaces* **2018**, *10*, 17933−17941.
(46) Lincoln, K. M.; Gonzalez, P.; Richardson, T. E.; Julovich, D. A.; Saunders, R.; Simpkins, J. W.; Green, K. N. A potent antioxidant small molecule aimed at targeting metal-based oxidative stress in neurodegenerative disorders. *Chem. Commun.* **2013**, *49*, 2712−2714.
(47) Lincoln, K. M.; Offutt, M. E.; Hayden, T. D.; Saunders, R. E.; Green, K. N. Structural, Spectral, and Electrochemical Properties of Nickel(II), Copper(II), and Zinc(II) Complexes Containing 12-Membered Pyridine- and Pyridol-Based Tetra-aza Macrocycles. *Inorg. Chem.* **2014**, *53*, 1406−1416.
(48) Yepremyan, A.; Mekhail, M. A.; Niebuhr, B. P.; Pota, K.; Sadagopan, N.; Schwartz, T. M.; Green, K. N. Synthesis of 12-Membered Tetra-aza Macrocyclic Pyridinophanes Bearing Electron-Withdrawing Groups. *J. Org. Chem.* **2020**, *85*, 4988−4998.
(49) The iodine number (I_N) was introduced to compare the iodine density within different crystalline phases. It was defined as the ratio between the number of iodine atoms per $Å^3$ of the crystal under examination and the number of iodine atoms per $Å^3$ of crystalline molecular iodine (ref 29).
(50) García-España, E.; Ballester, M. J.; Lloret, F.; Moratal, J. M.; Faus, J.; Bianchi, A. Low-spin six-co-ordinate cobalt(II) complexes. A solution study of tris(violurato)cobaltate(II) ions, Low-spin six-co-ordinate cobalt(II) complexes. A solution study of tris(violurato)-cobaltate(II) ions. *J. Chem. Soc., Dalton Trans.* **1988**, *2*, 101−104.
(51) Fontanelli, M.; Micheloni, M. In *Proceedings of the I Spanish-Italian Congress on Thermodynamics of Metal Complexes*; Diputación de Castellón: Castellón, Spain, 1990.
(52) Savastano, M.; Fiaschi, M.; Ferraro, G.; Gratteri, P.; Mariani, P.; Bianchi, A.; Bazzicalupi, C. Sensing Zn^{2+} in Aqueous Solution with a Fluorescent Scorpiand Macrocyclic Ligand Decorated with an Anthracene Bearing Tail. *Molecules* **2020**, *25*, 1355.
(53) Gran, G. Determination of the equivalence point in potentiometric titrations. Part II. *Analyst* **1952**, *77*, 661−671.
(54) Rossotti, F. J. C.; Rossotti, H. Potentiometric titrations using Gran plots: A textbook omission. *J. Chem. Educ.* **1965**, *42*, 375.
(55) Gans, P.; Sabatini, A.; Vacca, A. Investigation of equilibria in solution. Determination of equilibrium constants with the HYPERQUAD suite of programs. *Talanta* **1996**, *43*, 1739−1753.
(56) Alderighi, L.; Gans, P.; Ienco, A.; Peters, D.; Sabatini, A.; Vacca, A. Hyperquad simulation and speciation (HySS): a utility program for the investigation of equilibria involving soluble and partially. *Coord. Chem. Rev.* **1999**, *184*, 311−318.
(57) Delgado, R.; Da Silva, J. J. R. F.; Amorim, M. T. S.; Cabral, M. F.; Chaves, S.; Costa, J. Dissociation constants of Brønsted acids in D_2O and H_2O: studies on polyaza and polyoxa-polyaza macrocycles and a general correlation. *Anal. Chim. Acta* **1991**, *245*, 271−282.
(58) Arena, G.; Gans, P.; Sgarlata, C. HypCal, a general-purpose computer program for the determination of standard reaction enthalpy and binding constant values by means of calorimetry. *Anal. Bioanal. Chem.* **2016**, *408*, 6413−6422.
(59) Krause, L.; Herbst-Irmer, R.; Sheldrick, G. M.; Stalke, D. Comparison of silver and molybdenum microfocus X-ray sources for single-crystal structure determination. *J. Appl. Crystallogr.* **2015**, *48*, 3−10.
(60) Schneider, T. R.; Sheldrick, G. M. Substructure solution with SHELXD. *Acta Crystallogr., Sect. D: Biol. Crystallogr.* **2002**, *D58*, 1772−177.
(61) Sheldrick, G. M. SHELXT - Integrated space-group and crystal-structure determination. *Acta Crystallogr., Sect. A: Found. Adv.* **2015**, *A71*, 3−8.
(62) Sheldrick, G. M. Crystal structure refinement with SHELXL. *Acta Crystallogr., Sect. C: Struct. Chem.* **2015**, *C71*, 3−8.
(63) Spackman, M. A.; McKinnon, J. J. Fingerprinting intermolecular interactions in molecular crystals. *CrystEngComm* **2002**, *4*, 378−392.
(64) Spackman, M. A.; Byrom, P. G. A novel definition of a molecule in a crystal. *Chem. Phys. Lett.* **1997**, *267*, 215−220.

(65) McKinnon, J. J.; Spackman, M. A.; Mitchell, A. S. Novel tools for visualizing and exploring intermolecular interactions in molecular crystals. *Acta Crystallogr., Sect. B: Struct. Sci.* **2004**, *60*, 627−668.
(66) Turner, M. J.; McKinnon, J. J.; Wolff, S. K.; Grimwood, D. J.; Spackman, P. R.; Jayatilaka, D.; Spackman, M. A. *CrystalExplorer17*; University of Western Australia: Perth, Australia, 2017.
(67) Perdew, J. P. Density-functional approximation for the correlation energy of the inhomogeneous electron gas. *Phys. Rev. B: Condens. Matter Mater. Phys.* **1986**, *33*, 8822−8824.
(68) Becke, A. D. Density-functional exchange-energy approximation with correct asymptotic behavior. *Phys. Rev. A: At., Mol., Opt. Phys.* **1988**, *38*, 3098−3100.
(69) Lee, C.; Yang, W.; Parr, R. G. Development of the Colle-Salvetti correlation-energy formula into a functional of the electron density. *Phys. Rev. B: Condens. Matter Mater. Phys.* **1988**, *37*, 785−789.
(70) Weigend, F.; Ahlrichs, R. Balanced basis sets of split valence, triple zeta valence and quadruple zeta valence quality for H to Rn: Design and assessment of accuracy. *Phys. Chem. Chem. Phys.* **2005**, *7*, 3297−3305.
(71) Tomasi, J.; Mennucci, B.; Cammi, R. Quantum Mechanical Continuum Solvation Models. *Chem. Rev.* **2005**, *105*, 2999−3093.
(72) Frisch, M. J.; Trucks, G. W.; Schlegel, H. B.; Scuseria, G. E.; Robb, M. A.; Cheeseman, J. R.; Scalmani, G.; Barone, V.; Petersson, G. A.; Nakatsuji, H.; Li, X.; Caricato, M.; Marenich, A.; Bloino, J.; Janesko, B. G.; Gomperts, R.; Mennucci, B.; Hratchian, H. P.; Ortiz, J. V.; Izmaylov, A. F.; Sonnenberg, J. L.; Williams-Young, D.; Ding, F.; Lipparini, F.; Egidi, F.; Goings, J.; Peng, B.; Petrone, A.; Henderson, T.; Ranasinghe, D.; Zakrzewski, V. G.; Gao, J.; Rega, N.; Zheng, G.; Liang, W.; Hada, M.; Ehara, M.; Toyota, K.; Fukuda, R.; Hasegawa, J.; Ishida, M.; Nakajima, T.; Honda, Y.; Kitao, O.; Nakai, H.; Vreven, T.; Throssell, K.; Montgomery, J. A., Jr; Peralta, J. E.; Ogliaro, F.; Bearpark, M.; Heyd, J. J.; Brothers, E.; Kudin, K. N.; Staroverov, V. N.; Keith, T.; Kobayashi, R.; Normand, J.; Raghavachari, K.; Rendell, A.; Burant, J. C.; Iyengar, S. S.; Tomasi, J.; Cossi, M.; Millam, J. M.; Klene, M.; Adamo, C.; Cammi, R.; Ochterski, J. W.; Martin, R. L.; Morokuma, K.; Farkas, O.; Foresman, J. B.; Fox, D. J. *Gaussian 09, Revision A.02*, Gaussian, Inc.: Wallingford, CT, 2016.
(73) Schaftenaar, G.; Noordik, J. H. Molden: a pre- and post-processing program for molecular and electronic structures. *J. Comput.-Aided Mol. Des.* **2000**, *14*, 123−134.
(74) Pettersen, E. F.; Goddard, T. D.; Huang, C. C.; Couch, G. S.; Greenblatt, D. M.; Meng, E. C.; Ferrin, T. E. UCSF Chimera - a visualization system for exploratory research and analysis. *J. Comput. Chem.* **2004**, *25*, 1605−1612.
(75) Bencini, A.; Bianchi, A.; Giorgi, C.; Paoletti, P.; Valtancoli, B.; Fusi, V.; García-España, E.; Llinares, J. M.; Ramírez, J. A. Effect of Nitrogen Methylation on Cation and Anion Coordination by Hexa- and Heptaazamacrocycles. Catalytic Properties of These Ligands in ATP Dephosphorylation. *Inorg. Chem.* **1996**, *35*, 1114−1120.
(76) Martínez-Camarena, A.; Delgado-Pinar, E.; Soriano, C.; Alarcón, J.; Llinares, J. M.; Tejero, R.; García-España, E. Enhancement of SOD activity in boehmite supported nanoreceptors. *Chem. Commun.* **2018**, *54*, 3871−3874.
(77) Kortüm, G.; Vogel, W.; Andrussow, K. Dissociation constants of organic acids in aqueous solution. *Pure Appl. Chem.* **1960**, *1*, 187−536.
(78) GEMS (GEneral Microspeciation Solver) program, Blasco, S. 2019. Blasco, S.; Inclán, M.; Verdejo, B.; García-España, E. In *Acta of the International Symposia on Thermodynamics of Metal Complexes*; University of Białystok: Białystok, Poland, 2021. For the cluster expansion method see: Borkovec, M.; Koper, G. J. M. A Cluster Expansion Method for the Complete Resolution of Microscopic Ionization Equilibria from NMR Titrations. *Anal. Chem.* **2000**, *72*, 3272−3279.
(79) Bencini, A.; Bianchi, A.; García-España, E.; Micheloni, M.; Ramírez, J. A. Proton coordination by polyamine compounds in aqueous solution. *Coord. Chem. Rev.* **1999**, *188*, 97−156.
(80) Bianchi, A.; Escuder, B.; García-España, E.; Luis, S. V.; Marcelino, V.; Miravet, J. F.; Ramírez, J. A. Protonation tendencies of azaparacyclophanes. A thermodynamic and NMR study. *J. Chem. Soc., Perkin Trans. 2* **1994**, 1253−1259.
(81) Smith, R. M.; Martell, A. E. *NIST Stability Constants Database*, version 4.0; National Institute of Standards and Technology: Gaithersburg, MD, 1997.
(82) Hu, J.; Zhou, J.; Cao, S. An unusual cuprous iodide polymer incorporating I^-, I_2 and I_3^- structural units. *Dalton Trans.* **2018**, *47*, 17216−17220.
(83) Gilli, G.; Gilli, P. *The Nature of the Hydrogen Bond*; Oxford University Press, Oxford, 2009.
(84) Coppens, P. In *Extended Linear Chain Compounds*; Miller, J. S., Ed.; Plenum Press: New York, 1982; Vol. *1*, p 333.
(85) Savastano, M.; Bazzicalupi, C.; Gellini, C.; Bianchi, A. Genesis of Complex Polyiodide Networks: Insights on the Blue Box/I^-/I_2 Ternary System. *Crystals* **2020**, *10*, 387.
(86) Savastano, M.; Bazzicalupi, C.; Bianchi, A. Porous Frameworks Based on Supramolecular Ball Joints: Bringing Flexibility to Ordered 3D Lattices. *Chem. - Eur. J.* **2020**, *26*, 5994−6005.
(87) Schottel, B. L.; Chifotides, H. T.; Dunbar, K. R. Anion-π interactions. *Chem. Soc. Rev.* **2008**, *37*, 68−83.
(88) Bauzá, A.; Mooibroek, T. J.; Frontera, A. The Bright Future of Unconventional σ/π-Hole Interactions. *ChemPhysChem* **2015**, *16*, 2496−2517.
(89) Savastano, M.; García-Gallarín, C.; López de la Torre, M. D.; Bazzicalupi, C.; Bianchi, A.; Melguizo, M. Anion-π and lone pair-π interactions with *s*-tetrazine-based ligands. *Coord. Chem. Rev.* **2019**, *397*, 112−137.
(90) Wheeler, S. E.; Bloom, J. W. G. Anion-π interactions and positive electrostatic potentials of N-heterocycles arise from the positions of the nuclei, not changes in the π-electron distribution. *Chem. Commun.* **2014**, *50*, 11118−11121.
(91) Savastano, M.; Bazzicalupi, C.; Giorgi, C.; García-Gallarín, C.; López de la Torre, M. D.; Pichierri, F.; Bianchi, A.; Melguizo, M. Anion Complexes with Tetrazine-Based Ligands: Formation of Strong Anion-π Interactions in Solution and in the Solid State. *Inorg. Chem.* **2016**, *55*, 8013−8024.
(92) Savastano, M.; Bazzicalupi, C.; Mariani, P.; Bianchi, A. Network Formation via Anion Coordination: Crystal Structures Based on the Interplay of Non-Covalent Interactions. *Molecules* **2018**, *23*, 572.
(93) Savastano, M.; Bazzicalupi, C.; García-Gallarín, C.; Giorgi, C.; López de la Torre, M. D.; Pichierri, F.; Bianchi, A.; Melguizo, M. Halide and hydroxide anion binding in water. *Dalton Trans.* **2018**, *47*, 3329−3338.
(94) Savastano, M.; Bazzicalupi, C.; García, C.; Gellini, C.; López de la Torre, M. D.; Mariani, P.; Pichierri, F.; Bianchi, A.; Melguizo, M. Iodide and triiodide anion complexes involving anion-π interactions with a tetrazine-based receptor. *Dalton Trans.* **2017**, *46*, 4518−4529.
(95) Savastano, M.; García, C.; López de la Torre, M. D.; Pichierri, F.; Bazzicalupi, C.; Bianchi, A.; Melguizo, M. Interplay between salt bridge, hydrogen bond and anion-π interactions in thiocyanate binding. *Inorg. Chim. Acta* **2018**, *470*, 133−138.
(96) Savastano, M.; García-Gallarín, C.; Giorgi, C.; Gratteri, P.; López de la Torre, M. D.; Bazzicalupi, C.; Bianchi, A.; Melguizo, M. Solid State and Solution Study on the Formation of Inorganic Anion Complexes with a Series of Tetrazine-Based Ligands. *Molecules* **2019**, *24*, 2247.
(97) Savastano, M.; Bazzicalupi, C.; García-Gallarín, C.; López de la Torre, M. D.; Bianchi, A.; Melguizo, M. Supramolecular forces and their interplay in stabilizing complexes of organic anions: tuning binding selectivity in water. *Org. Chem. Front.* **2019**, *6*, 75−86.
(98) Göth, M.; Witte, F.; Quennet, M.; Jungk, P.; Podolan, G.; Lentz, D.; Hoffmann, W.; Pagel, K.; Reissig, H.-U.; Paulus, B.; Schalley, C. A. To Anion-π or not to Anion-π: The Case of Anion-Binding to Divalent Fluorinated Pyridines in the Gas Phase. *Chem. - Eur. J.* **2018**, *24*, 12879−12889.
(99) Hoque, M. N.; Manna, U.; Das, G. Discrepancy in anion coordination directed by isomeric pyridine-urea receptors: Solid state recognition of hydrated anions. *Polyhedron* **2016**, *119*, 307−316.

(100) de Hoog, P.; Robertazzi, A.; Mutikainen, I.; Turpeinen, U.; Gamez, P.; Reedijk, J. An Electron-Poor Host Receptor for Electron-Rich Guests Involving Anion-π and Lone-Pair-π Interactions. *Eur. J. Inorg. Chem.* **2009**, *2009*, 2684−2690.

https://doi.org/10.1021/acs.inorgchem.1c02967
Inorg. Chem. 2022, 61, 368−383